Journal of Magnetic Resonance **154,** 210–227 (2002)
doi:10.1006/jmre.2001.2472, available online at http://www.idealibrary.com on IDEAL®

# Probe–Sample Coupling in the Magnetic Resonance Force Microscope

A. Suter,*[,1] D. V. Pelekhov,* M. L. Roukes,† and P. C. Hammel*

*Condensed Matter and Thermal Physics, Los Alamos National Laboratory, Los Alamos, New Mexico 87545; and †Condensed Matter Physics, Caltech, Pasadena, California

E-mail: andreas.suter@psi.ch, pch@lanl.gov

Received April 30, 2001; revised October 30, 2001

**The magnetic resonance force microscope (MRFM) provides a route to achieving scanned probe magnetic resonance imaging with extremely high spatial resolution. Achieving this capability will require understanding the force exerted on a microscopic magnetic probe by a spatially extended sample over which the probe is scanned. Here we present a detailed analysis of this interaction between probe and sample. We focus on understanding the situation where the micromagnet mounted on the mechanical resonator generates a very inhomogeneous magnetic field and is scanned over a sample with at least one spatial dimension much larger than that of the micromagnet. This situation differs quite significantly from the conditions under which most MRFM experiments have been carried out where the sample is mounted on the mechanical resonator and placed in a rather weak magnetic field gradient. In addition to the concept of a sensitive slice (the spatial region where the magnetic resonance condition is met) it is valuable to map the forces exerted on the probe by spins at various locations; this leads to the concept of the force slice (the region in which spins exert force on the resonator). Results of this analysis, obtained both analytically and numerically, will be qualitatively compared with an initial experimental finding from an EPR-MRFM experiment carried out on DPPH at 4 K.** 

*Key Words*: **MRFM, magnetic resonance force microscope; sensitive slice; scanned probe microscopy.**

## 1. INTRODUCTION

Improving the sensitivity of detection in electronic paramagnetic resonance (EPR) and nuclear magnetic resonance (NMR) has been an important focus of efforts to broaden the power of magnetic resonance techniques. A remarkable variety of approaches have been taken including those exploiting optical pumping and detection (*1–3*) or SQUID detection of NMR signals (*4*), to mention a few.

A very different approach has been proposed by Sidles (*5, 6*). He realized that a magnetic moment can be coupled to a mechanical detector in the presence of a gradient of the magnetic induction:

$$\boldsymbol{F}(\boldsymbol{r}, t) = -[\boldsymbol{m}(\boldsymbol{r}, t) \cdot \nabla]\boldsymbol{B}_{\text{tot}}(\boldsymbol{r}) \qquad [1]$$

The force signal is proportional to the magnetic field gradient; this can be made very large and provide very high detection sensitivity and thus high spatial resolution. An instrument based on this idea is referred to as a magnetic resonance force microscope (MRFM) (*6*). A sketch of an MRFM employing a micromagnet mounted on a mechanical resonator as the source of the magnetic gradient is shown in Fig. 1. Another approach is to place the sample on the mechanical resonator, which is placed in an inhomogeneous magnetic field.

The first magnetic resonance force signal was detected by Rugar *et al.*, in 1992 who mechanically detected the electron spin resonance signal (eMRFM) from a 30 ng crystal of diphenylpicrylhydrazil (*7*). Two years later, Rugar *et al.* reported the mechanical detection of $^1$H nuclear magnetic resonance (nMRFM) in 12 ng of ammonium nitrate (*8*). These two pioneering experiments demonstrated that a microfabricated cantilever, similar to those developed for atomic force microscopy, can detect the magnetic moment of a microscopic sample. In the case of nuclear magnetic resonance (NMR) (*8*), the achieved sensitivity of $10^{13}$ spins at room temperature and in a field of 2.4 T represents a substantial improvement over the standard coil detection sensitivity.

Significant progress has been made in the past few years. In 1996, Zhang *et al.* mechanically detected ferromagnetic resonance signals (fMRFM) of yttrium iron garnet (*9*). Imaging experiments with eMRFM (*10, 11*), nMRFM (*12, 13*), and fMRFM (*14*) were performed. A magnetic resonance torque signal in a homogeneous magnetic field (*15*) was also detected. Improved force sensitivity was demonstrated by operating at low temperature (*16–18*). Force maps of a sample were obtained with the magnetic probe placed on the mechanical resonator in eMRFM (*19*) and fMRFM (*14*). The highest sensitivity reported to date is ~200 electron spins in a 1 Hz bandwidth. The result was obtained by operating an eMRFM at 77 K in a very large magnetic field gradient (*20*). In 1996, Wago *et al.* demonstrated that

[1] Present address: Laboratory for Muon-Spin Spectroscopy (LMU) Paul Scherrer Institut CH-5232 Villigen PSI Switzerland.

1090-7807/02 $35.00

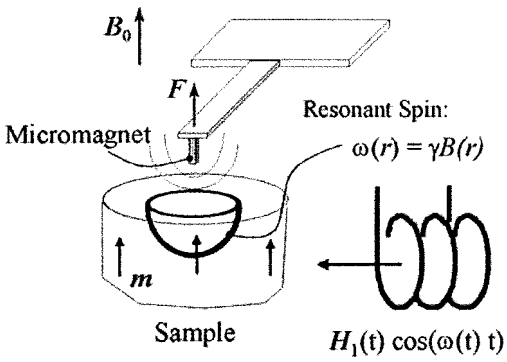


**FIG. 1.** Sketch of an MRFM. The micromagnet on the mechanical resonator produces an extremely inhomogeneous magnetic field that serves two purposes: (i) It couples the mechanical resonator to the magnetic moments in the sample, and (ii) it defines the spatial regions of the sample where the magnetic resonance condition is met. Magnetic resonance techniques can be employed to manipulate the magnetization $m$ thus generating a force on the mechanical resonator at its resonance frequency that will drive it into oscillation.

combining pulsed NMR techniques with fast adiabatic passage enables measurement of the nuclear spin–lattice relaxation rate, which they demonstrated for $^{19}$F nuclear moments in calcium fluoride at low temperature (*16*). The same method was used to measure the longitudinal spin relaxation of $^{1}$H rate in ammonium sulfate at room temperature (*21, 22*). Klein *et al.* (*23*) were able to demonstrate two different $T_1$'s in a microscopic crystallite of ammonium sulfate, one attributed to spins in the surface layer of the crystal. They also measured the spin–spin relaxation time $T_2$ of protons. Recent eMRFM work in vitreous silica at 5 K showed that the same principles can be also applied to study electron angular momentum dynamics of slowly relaxing E' centers (*18*).

In most of the work cited above the sample was placed on the mechanical resonator and operated in an externally applied magnetic field gradient of rather small magnitude. This situation corresponds to Fig. 1 except that the location of the sample and the gradient magnet are interchanged. The external magnetic field gradient is generally produced by a permanent magnet placed close the sample and its spatial dimensions are typically much larger than the sample. This leads to a rather simple probe–sample coupling since the sensitive slice, i.e., the region (a surface of constant magnetic field) where the magnetic resonance condition is fulfilled, can be well approximated by a paraboloid (*24*). The disadvantage of this setup is twofold: (i) The strength of the magnetic field gradient and hence the sensitivity is rather limited. (ii) The sample must be mounted on the mechanical resonator; this dramatically limits the range of samples that can be studied and reduces the quality factor of the detector thereby limiting sensitivity. It further limits the range of possible mechanical resonators which can be used, since they must have spatial dimensions much larger than the sample. Clearly the arrangement sketched in Fig. 1 is essential for a useful microscope. However the price to be paid when working with the micromagnet on the mechanical resonator is a significantly more complex interaction between the probe and sample; this will be the subject of the present manuscript.

This complication arises because the force exerted on the detector is proportional to the magnetic field gradient whose magnitude and orientation varies dramatically throughout the sensitive slice. A complete analytical analysis of the probe–sample interaction for general experimental MRFM geometries is quite complicated, however solutions to symmetric limiting cases were found which prove to be valuable guides for understanding this interaction. For quantitative comparisons with the experiment, numerical simulations of the probe–sample interaction will be given. The main advantage of this approach is that the analysis of an arbitrary probe sample geometry is possible, and more realistic models of the micromagnet can be implemented.

The main body of the paper is organized as follows: In Section 2 we introduce the model and subsequently derive the analytical solutions for different limiting cases. Section 3 describes the algorithm used for the numerical evaluation for more realistic parameters, and Sections 4 presents a brief description of experimental measurements to test our modeling. These results are discussed in Section 5.

## 2. DESCRIPTION OF THE PROBE–SAMPLE INTERACTION

In the following we will derive our model of the probe–sample interaction. This model is rather general and is capable of describing the probe–sample interaction in the limit of an extended sample, i.e., where the sample is much larger then the micromagnet. Understanding this situation is essential if we are to use the MRFM as a scanning tool. As will be demonstrated below this situation leads to some counterintuitive results; these will be thoroughly discussed in Section 5. A particularly important result is that the concept of the sensitive slice must be reexamined. The slice width $x_{\mathrm{sl}}$ is determined by the intrinsic homogeneous line width $\delta B$ and the magnitude of the field gradient $|\nabla B|$ (generated by the micromagnet) at the particular location of the spin whose coupling is under consideration: $x_{\mathrm{sl}} \approx \delta B/|\nabla B|$; because of the spatial variation of $|\nabla B|$, the concept of a length scale set by $x_{\mathrm{sl}}$ breaks down under some conditions met in probe-on-detector measurements.

In order to calculate the resonant response of the mechanical resonator, we will proceed as follows: First we will derive formulae for the local field, i.e., the superposition of all the involved fields. This is necessary since its magnitude will determine the spatial volume in which the resonance condition is met, or in other words the spatial dependence of the resonance frequency. Furthermore this allows us to determine the correct field component relevant for the force coupling to the mechanical resonator according to Eq. [1]. To do so we will use a dipolar approximation for the micromagnet. For most of the experimentally useful geometries this should be a satisfactory approximation. Next, we will determine the local magnetization, which together with the field allows us to calculate the *local* force stemming from a volume element $d^3x$ at an arbitrary position $\boldsymbol{r}$. At this point we

would like to stress that the sensitive slice (region in space where the resonance condition is fulfilled) and the force slice (spatial map of the force exerted the mechanical resonator at its resonance frequency) are related by Eq. [1], however they are *not* synonymous due to the variation of the magnitude and sign of the relevant component of the field gradient. The consequences of this distinction are striking and will be discussed in Section 5. Finally, the total force acting on the mechanical resonator is the integral of the local force over the entire sample.

It is not possible to carry out this spatial integration analytically for the most general case, so after generating general expressions from the model we restrict our analysis to a few specific cases, namely: In Section 2.1 we solve it in the case where the magnetization is described by a homogeneous intrinsic Lorentzian line shape. To do so we restrict the sample geometry to a semi-infinite sample and apply some further restrictions. In order to be able to treat more general sample geometries and to loosen these further restrictions, we also calculate the force response for a rectangular line shape; this is presented in Section 2.2 and 2.3. Section 2.2 presents a semiinfinite sample geometry, while Section 2.3 presents the force response from a buried thin layer.

For all these cases we assume that the spin–lattice relaxation time $T_1$ is much shorter than the inverse frequency of the mechanical resonator $1/\omega_{\mathrm{mr}}$. Under these conditions we can employ rf-modulation schemes (amplitude and frequency modulation) (*25*) which generate a time dependent magnetization with a strong Fourier component at the resonance frequency of the mechanical resonator. Furthermore the magnetization can always be assumed to be in dynamical equilibrium on the time scale $1/\omega_{\mathrm{mr}}$.

What about the opposite limit where $T_1 \gg 1/\omega_{\mathrm{mr}}$? In this situation one can manipulate the spin system utilizing fast adiabatic inversion schemes resulting in an efficient coupling at the resonance frequency of the mechanical resonator. We will not discuss this limit here but the qualitative picture we are going to discuss is not altered. This is true since the observed resonant displacement of the mechanical resonator is still describable in a rather similar fashion. Most of the features described below originate from the coupling of a micromagnetic tip to a spin volume larger then the micromagnet.

With this overview in mind, we now present our model. The force originating at some point in space due to the presence of a given magnetization interacting with an inhomogeneous magnetic induction is given as

$$\begin{aligned}\boldsymbol{F}(\boldsymbol{r},t) &= -[m(\boldsymbol{r},t)\cdot\nabla]\boldsymbol{B}_{\mathrm{tot}}(\boldsymbol{r}) \\ &= -\nabla'[m(\boldsymbol{r},t)\cdot\boldsymbol{B}_{\mathrm{tot}}(\boldsymbol{r})] \end{aligned} \quad [2]$$

where $\nabla'$ acts *only* on $\boldsymbol{B}_{\mathrm{tot}}(\boldsymbol{r})$ and the total magnetic induction decomposes into

$$\boldsymbol{B}_{\mathrm{tot}}(\boldsymbol{r}) = \boldsymbol{B}_0 + \boldsymbol{B}(\boldsymbol{r}) + \boldsymbol{B}_{\mathrm{local}}(\boldsymbol{r}) \quad [3]$$

where $\boldsymbol{B}_0$ is the external polarizing magnetic induction, $\boldsymbol{B}(\boldsymbol{r})$ is the magnetic induction due to the micromagnetic on the mechanical resonator and $\boldsymbol{B}_{\mathrm{local}}(\boldsymbol{r})$ induction resulting from any other source experienced by the local magnetization, such as, e.g., magnetic dipole fields of spins within the sample. In the following we will suppress $\boldsymbol{B}_{\mathrm{local}}(\boldsymbol{r})$ assuming it to be much smaller than $\boldsymbol{B}_0$ and $\boldsymbol{B}(\boldsymbol{r})$.

In the following we will use the dipolar approximation for the magnetic induction generated by the micromagnet

$$\boldsymbol{B}(\boldsymbol{r}) = 2B(r)\cos(\theta)\boldsymbol{e}_{\boldsymbol{r}} + B(r)\sin(\theta)\boldsymbol{e}_{\theta} \quad [4]$$

with

$$B(r) = B_m\left(\frac{R_s}{r}\right)^{\xi}. \quad [5]$$

In the case of a spherical, homogeneously magnetized sphere, $B_m = \frac{4\pi}{3}M_0$ with $M_0$ the saturation magnetization, $R_s$ the radius of the sphere, and $\xi = 3$. Numerical simulations of a realistic micromagnet suggest a $\xi < 3$, even though the real radial functional dependence is no longer purely power-law.

For our calculations we will use the geometry shown in Fig. 2. The total magnetic field is then given as

$$\begin{aligned}\boldsymbol{B}_{\mathrm{tot}} &= \boldsymbol{B}_0 + \boldsymbol{B}(\boldsymbol{r}) \\ &= \boldsymbol{e}_{\boldsymbol{x}}\frac{3}{2}B(r)\sin(2\theta)\cos(\phi) + \boldsymbol{e}_{\boldsymbol{y}}\frac{3}{2}B(r)\sin(2\theta)\sin(\phi) \\ &\quad + \boldsymbol{e}_{\boldsymbol{z}}\left[B_0 + \frac{B(r)}{2}(3\cos(2\theta)+1)\right], \end{aligned} \quad [6]$$

so the spatial variation of the angular resonance frequency is

$$\begin{aligned}\frac{\omega_S(r,\theta)}{\gamma} &= |\boldsymbol{B}_{\mathrm{tot}}| \\ &= B_0\left[1 + \frac{B(r)}{B_0}(3\cos(2\theta)+1) + \frac{1}{2}\left(\frac{B(r)}{B_0}\right)^2\right. \\ &\quad \left.\times(3\cos(2\theta)+5)\right]^{1/2} \\ &= B_0\left[1 + \frac{B(r)}{2B_0}(3\cos(2\theta)+1)\right] + \mathcal{O}\left(\frac{B(r)}{B_0}\right)^2 \end{aligned} \quad [7]$$

Because we assume $1/T_1 \gg \omega_{\mathrm{mr}}/2\pi$, we can achieve an effective coupling to the mechanical resonator at its resonance frequency by cyclic suppression of the magnetization. This can experimentally be accomplished in at least three ways: (i) Amplitude modulation of $B_0$; (ii) Amplitude Modulation of the rf-field; or (iii) Frequency Modulation of the rf-field. For all these cases the magnetization in the laboratory reference frame

is approximately

$$m(r,t) = \boldsymbol{e}_z m_0 \mathcal{L}(\boldsymbol{r},t) \quad [8]$$

where $m_0$ is the magnetization density and $\mathcal{L}(\boldsymbol{r},t)$ is the normalized intrinsic magnetic resonance lineshape under consideration. The time dependence of $\mathcal{L}$ and hence $F_z$ is to be understood in the following way. Since we only consider the situation $1/T_1 \gg \omega_{\rm mr}/2\pi$, the magnetization density is *always* in dynamical equilibrium with the rf-field and hence will accurately follow variations in the rf-field (AM, FM) which are slow compared to $\omega_{\rm rf}$.

Since the mechanical resonator only couples to the $z$-component of the force field Eq. [2] gets together with Eqs. [6] and [8].

$$\begin{aligned} F_z(\boldsymbol{r},t) &= \boldsymbol{F}(\boldsymbol{r},t)\cdot\boldsymbol{e}_z \\ &= -m_0\mathcal{L}(\boldsymbol{r},t)\left[\frac{\partial B(r)}{\partial r}\frac{1}{2}(3\cos(2\theta)+1)\cos(\theta)\right. \\ &\quad \left. + \frac{B(r)}{r}3\sin(2\theta)\sin(\theta)\right]. \end{aligned} \quad [9]$$

This is the force from the volume element $d^3x$ acting on the mechanical resonator. A key point is that the sign of this local force depends on position $\boldsymbol{r}$; this is also sketched in Fig. 2. Starting with Eqs. [5] and [9] one can find an analytical expression for the angle $\theta_c$ at which the force vanishes, namely

$$\theta_c = \pi - \arccos\left(\sqrt{\frac{6+\xi}{6+3\xi}}\right). \quad [10]$$

The total force from a semiinfinite sample experienced by the mechanical resonator is

$$F_{\rm tot}(t) = \int_a^\infty r^2\,dr \int_{\vartheta(r)}^{\pi} \sin(\theta)\,d\theta \int_0^{2\pi} d\phi\, F_z(\boldsymbol{r},t). \quad [11]$$

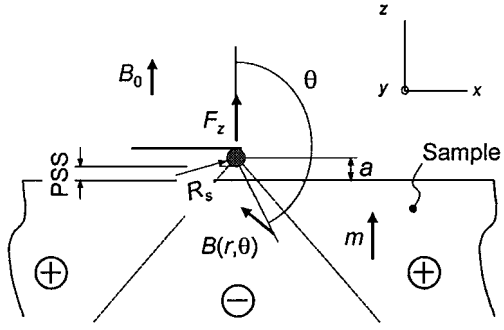


**FIG. 2.** Geometry used in the calculations. The sphere represents the micromagnet on the mechanical resonator. Since we use a dipole approximation in our calculations, spherical coordinates are used. The dashed line separates regions of negative and positive force coupling as indicated by $\ominus$ and $\oplus$.

$\vartheta(r)$ is the angle beyond which a radial line originating at the probe magnet first intersects the sample. To calculate this integral we use the variables

$$\begin{aligned} x &\equiv 3\cos(2\theta)+1 \\ B &\equiv B_m\left(\frac{R_s}{r}\right)^{\xi}. \end{aligned} \quad [12]$$

Equation [11] can then be written

$$\begin{aligned} F_{\rm tot}(t) = 2\pi m_0 \frac{R_s^2}{24\xi}\int_{-2}^{4} dx \int_0^{B_c(x)} dB\,\mathcal{L}(B,x,t)\left(\frac{B_m}{B}\right)^{2/\xi} \\ \times[8-(2+\xi)x]. \end{aligned} \quad [13]$$

Here $B_c(x)$ is the magnetic induction at the point where a radial line originating at the probe with angle $\theta$ intersects the surface of the sample

$$B_c(x) = B_m\left(\frac{x+2}{6\kappa_c}\right)^{\xi/2} \quad [14]$$

with $\kappa_c = (a/R_s)^2$, where $a$ is the distance from the centre of the spherical probe magnet to the surface (see Fig. 2).

The displacement $z(t)$ of the mechanical resonator is given by

$$z(t) = \int_0^t d\tau\; z_G(t-\tau)\frac{F_{\rm tot}(\tau)}{m} \quad [15]$$

with $m$ the mass of the mechanical resonator and

$$z_G(t) = \frac{e^{-\Gamma t}}{\omega_{\rm mr}}\sin(\omega_{\rm mr}t)$$

where $\Gamma \simeq \omega_{\rm mr}/(2Q)$ where $Q$ is the quality factor of the mechanical resonator. Since $Q$ is typically very large the strongest displacement response will stem from the $\omega_{\rm mr}$-Fourier component of $z(t)$.

Given the solution for the total force acting on the mechanical resonator, the displacement can be calculated from Eq. [15] and $z(\omega_{\rm mr})$ by Fourier transformation. However this leads to *very* complex results, whose interpretation is not transparent. Simplifications can be obtained by using approximate solutions and noting that: (i) The mechanical resonators used in these experiments have very high $Q$'s (of the order of $10^4$), and (ii) the displacement of the mechanical resonator is measured via interferometry and recorded with a lock-in amplifier (see Section 4). As a consequence we are only interested in the $\omega_{\rm mr}$ Fourier component of the steady state amplitude of $z(t)$. This allows the approximation

$$z(\omega_{\rm mr}) \simeq \frac{Q}{m\omega_{\rm mr}^2}\left[F_{\rm tot}(t=0) - F_{\rm tot}\left(t=\frac{\pi}{\omega_{\rm mr}}\right)\right] \quad [16]$$

where the time dependence of $F_{\text{tot}}(t)$ is to be understood in the following manner. Given that $1/T_1 \gg \omega_{\text{mr}}/(2\pi)$ the magnetization is always in equilibrium on the time scale of interest $1/\omega_{\text{mr}}$. Therefore the parameters in $F_{\text{tot}}$ can be assumed time dependent. In the following we will discuss amplitude modulation of the rf-field only; however we find that both frequency modulation of the rf-field and modulation of $B_0$ give very similar results. If $H_1$ is the amplitude of the rf-field and $\omega_1 = \gamma H_1$; amplitude modulation is described by

$$\omega_1^{(\text{AM})}(t) = \omega_1\left[1 + \frac{\zeta}{1+\zeta}\cos(\omega_{\text{mr}}t)\right], \qquad [17]$$

where $0 \le \zeta \le 1$ describes the depth of amplitude modulation.

Using these results, we can calculate the total force under different conditions. We integrate Eq. [13] for two different line shapes: a Lorentzian line shape such as given by the standard Bloch equations, and for a rectangular line shape. Obviously the rectangular line shape is unphysical, however this limit has the advantage of being more transparent, showing the physical essence in the probe–sample interaction. The solution for a thin magnetic layer will be presented for the rectangular line shape approximation only.

### *2.1. Lorentzian Line Shape*

We take $1/T_1 \gg \omega_{\text{mr}}/(2\pi)$, and are only interested in time scales of order $1/\omega_{\text{mr}}$, so we can use the steady state solution of the Bloch equation

$$\mathcal{L}(r,t) = \frac{1 + [\omega_{\text{rf}} - \omega_S(r,\theta)]^2 T_2^2}{1 + [\omega_{\text{rf}} - \omega_S(r,\theta)]^2 T_2^2 + \omega_1^2 T_1 T_2}, \qquad [18]$$

where $\omega_{\text{rf}}$ is the frequency of the irradiating rf-field, $T_1$ the spin–lattice relaxation time, and $T_2$ the spin–spin relaxation time, and we may consider the lineshape parameters to be time dependent.

This description of the magnetization is appropriate under the following conditions:

1. The relaxation rates are much faster than the angular resonance frequency of the mechanical resonator $\omega_{\text{mr}}$. This ensures that the magnetization is always in thermal equilibrium with the applied magnetic fields.
2. The local spin–spin interactions must be weak enough to allow the use of the Bloch equations.
3. The local field of the micromagnet $B(r)$ must be weak enough, that the deviation of the magnetization from $e_z$ is negligible.

Equation [13] can only be integrated in a closed form in the limit $B_c(x) \to B_m$. This situation is shown in Fig. 3: the sample has a small spherical dent of the size of the micromagnet and the micromagnet is located within this dent; we set $\xi = 2$. This

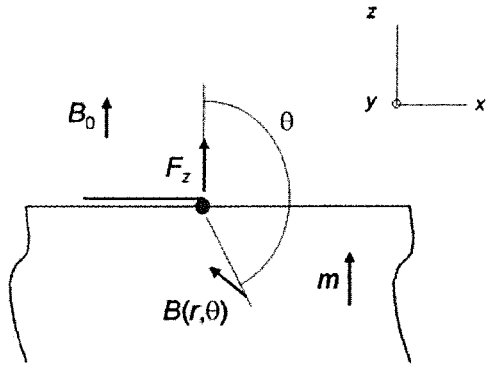


**FIG. 3.** Geometry used for calculating the case of a Lorentzian line shape. The center of the micromagnet is located at the sample surface. This simplifies the problem sufficiently that analytical solutions for the total force acting on the mechanical resonator can be found.

situation is not fully realistic but provides accurate insight into the magnetization dyanmics.

Under these highly symmetric conditions the solution of Eq. [13] is

$$F_{\text{tot}}(t) = 2\pi m_0 R_s^2\left[\alpha_0 + \sum_{k=1}^{3}\alpha_k \ln\left[1 + \omega_1^2 T_1 T_2 + T_2^2(\Delta\omega + (-1)^k(k-1)\omega_m)^2\right] + \beta_k \arctan\left(\frac{T_2(\Delta\omega + (-1)^k(k-1)\omega_m)}{\sqrt{1+\omega_1^2 T_1 T_2}}\right)\right] \qquad [19]$$

where $\omega_0 = \gamma B_0$, $\omega_m = \gamma B_m$ and the coefficients $\alpha_k$ and $\beta_k$ are given by

$$\alpha_0 = B_m \frac{3\omega_1^2 T_1 T_2 - 2\left(1 + \Delta\omega^2 T_2^2\right)\ln(B_m/1)}{4\left(1 + \omega_1^2 T_1 T_2 + \Delta\omega^2 T_2^2\right)}$$

$$\alpha_1 = B_m \frac{\omega_1^2 T_1 T_2}{4\left(1 + \omega_1^2 T_1 T_2 + \Delta\omega^2 T_2^2\right)}$$

$$\alpha_2 = (-1)\frac{H_1^2 T_1}{12 B_m T_2} \cdot \frac{1 + \omega_1^2 T_1 T_2 + \left(\Delta\omega^2 + 3\omega_m^2\right)T_2^2}{1 + \omega_1^2 T_1 T_2 + \Delta\omega^2 T_2^2}$$

$$\alpha_3 = \frac{H_1^2 T_1}{12 B_m T_2}$$

$$\beta_1 = B_m \frac{\omega_1^2 \Delta\omega T_1 T_2^2}{2\sqrt{1+\omega_1^2 T_1 T_2}\left(1 + \omega_1^2 T_1 T_2 + \Delta\omega^2 T_2^2\right)}$$

$$\beta_2 = \frac{H_1^2}{6 B_m} \cdot \frac{T_1\left(1 + T_1 T_2 \omega_1^2\right)(\Delta\omega - 2\omega_m) + T_1 T_2^2 \Delta\omega\left[(\Delta\omega - \omega_m)^2 - 4\omega_m^2\right]}{\sqrt{1+\omega_1^2 T_1 T_2}\left(1 + \omega_1^2 T_1 T_2 + \Delta\omega^2 T_2^2\right)}$$

$$\beta_3 = (-1)\frac{H_1^2}{6B_m}\cdot\frac{(\Delta\omega - 2\omega_m)T_1}{\sqrt{1+\omega_1^2 T_1 T_2}}$$

with $\Delta\omega = \omega_{\rm rf} - \omega_0$.

The implications of this result will be discussed in Section 5, along with the results for a rectangular line shape, the results of numerical simulations and comparisons with experimental findings.

### *2.2. Rectangular Line Shape*

To enable analytical solution for cases of lower symmetry, we will use a model where the line shape is approximated by a rectangle whose width and depth are obtained from the Bloch Eqs.

$$\mathcal{L}(x,B) = \begin{cases} 1, & |\Delta\omega_S| > \delta\omega \\ \mathcal{L}_r \equiv \frac{1}{1+\omega_1^2 T_1 T_2}, & |\Delta\omega_S| \le \delta\omega \end{cases} \qquad [20]$$

where $\Delta\omega_S$ (see Eqs. 7 and 12) is

$$\Delta\omega_S = \omega_{\rm rf} - \omega_S = \omega_{\rm rf} - \omega_0\left(1 + \frac{Bx}{2B_0}\right)$$

and the natural line width $\delta\omega = \sqrt{1+\omega_1^2 T_1 T_2}/T_2$. The boundary of the resonant region in the $(B,x)$-phase space is therefore given by

$$Bx = 2B_0\underbrace{\left(\frac{\omega_{\rm rf}\pm\delta\omega}{\omega_0} - 1\right)}_{\equiv A_\pm} \qquad [21]$$

The total force acting on the mechanical resonator is

$$F_{\rm tot} = -2\pi m_0\frac{R_s^2}{24\xi}\int\!\!\int_{\mathcal{R}} dx\,dB \times\left\{\mathcal{L}(x,B)\left(\frac{B_m}{B}\right)^{2/\xi}[8-(2+\xi)x]\right\} \qquad [22]$$

where $\mathcal{R}$ is the volume of the sample where the resonance condition is satisfied (sensitive slice). Different aspects of this arise from various spatial relationships between the sensitive slice and the sample. To keep the body of the paper compact, details of the discussion of these different cases are given in Section 5 and Appendix A.1. In Fig. 4 the different regions are labeled 1 to 7. Their physical meaning is as follows: In region 1 the external field is so small that the sensitive slice is outside the sample and hence there is no force coupling. In regions 2 and 3 the sensitive slice has just entered the sample with an onion-shell like structure; in 3 the full width of the slice has entered the sample. In region 4 most of the sample is going into resonance and the concept of a sensitive slice must be handled cautiously (see Section 5). Regions 5 and 6 are analogous to 2 and 3 except that the shape of the sensitive slice changes as we will discuss in Section 5. In region 7 the external field is so large that no part of the sample is resonant.

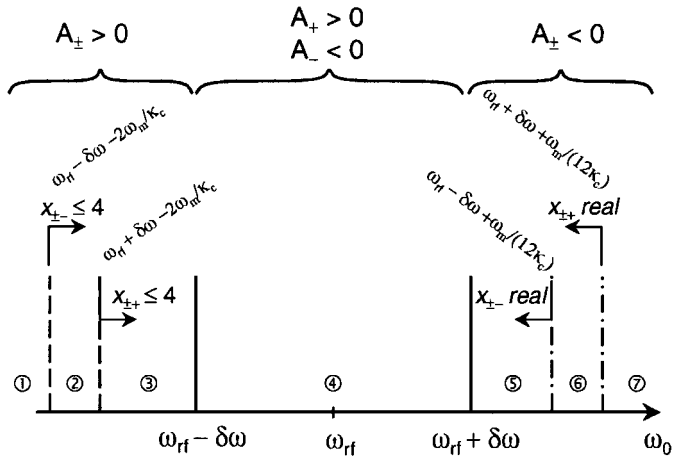


**FIG. 4.** The various regions of $B$-$x$ space vs $\omega_0$ (labeled 1 to 7 describing the evolution of the resonant region: At the border $1 \to 2$ the sensitive slice enters the sample; at the boundary it leaves the sample $6 \to 7$ (see also Appendix A.1).

If we define $\beta \equiv 2/\xi$, and

$$x_{\mp\pm} = -1 \mp \sqrt{1+\kappa_c\frac{12B_0A_\pm}{B_m}}, \qquad [23]$$

the force for the case $\omega_m/(12\kappa_c) > 2\delta\omega$ is

$$F_{\rm tot}^{(1)} = 0$$

$$F_{\rm tot}^{(2)} = -\frac{2\pi m_0 R_s^2\mathcal{L}_r}{\xi(\xi-2)}\left\{-\frac{B_0\xi^2}{3\cdot 2^{2+\beta}}\left(\frac{B_m}{B_0}\right)^\beta \times A_-(x_{+-}-4)\left(\frac{x_{+-}}{A_-}\right)^\beta + B_m\kappa_c^{1-1/\beta} \times\left[6-2\xi-\frac{(12-\xi x_{+-})(x_{+-}+2)^{1/\beta}}{2^{1+1/\beta}\cdot 3^{1/\beta}}\right]\right\}$$

$$F_{\rm tot}^{(3)} = -\frac{2\pi m_0 R_s^2\mathcal{L}_r}{\xi(\xi-2)}\left\{\frac{B_0\xi^2}{3\cdot 2^{2+\beta}}\left(\frac{B_m}{B_0}\right)^\beta \times\left[A_+(x_{++}-4)\left(\frac{x_{++}}{A_+}\right)^\beta - A_-(x_{+-}-4)\left(\frac{x_{+-}}{A_-}\right)^\beta\right] + \frac{B_m\kappa_c^{1-1/\beta}}{2^{1+\beta}\cdot 3^{1/\beta}}\left[(12-\xi x_{++})(x_{++}+2)^{1/\beta} - (12-\xi x_{+-})(x_{+-}+2)^{1/\beta}\right]\right\}$$

$$F_{\rm tot}^{(4)} = -\frac{2\pi m_0 R_s^2 \mathcal{L}_r}{\xi(\xi-2)}\left\{\frac{B_0\xi^2}{3\cdot 2^{2+\beta}}\left(\frac{B_m}{B_0}\right)^{\beta}\right.$$
$$\times\left[A_-(x_{--}-4)\left(\frac{x_{--}}{A_-}\right)^{\beta} - A_-(x_{+-}-4)\left(\frac{x_{+-}}{A_-}\right)^{\beta}\right.$$
$$\left.+A_+(x_{++}-4)\left(\frac{x_{++}}{A_+}\right)^{\beta}\right] + \frac{B_m\kappa_c^{1-1/\beta}}{2^{1+\beta}\cdot 3^{1/\beta}}$$
$$\times\left[(12-\xi x_{--})(x_{--}+2)^{1/\beta} - (12-\xi x_{+-})\right.$$
$$\left.\times(x_{+-}+2)^{1/\beta} + (12-\xi x_{++})(x_{++}+2)^{1/\beta}\right]\Bigg\} \qquad [24]$$

$$F_{\rm tot}^{(5)} = -\frac{2\pi m_0 R_s^2 \mathcal{L}_r}{\xi(\xi-2)}\left\{\frac{B_0\xi^2}{3\cdot 2^{2+\beta}}\left(\frac{B_m}{B_0}\right)^{\beta}\right.$$
$$\times\left[A_-(x_{--}-4)\left(\frac{x_{--}}{A_-}\right)^{\beta} - A_-(x_{+-}-4)\left(\frac{x_{+-}}{A_-}\right)^{\beta}\right.$$
$$\left.+A_+(x_{++}-4)\left(\frac{x_{++}}{A_+}\right)^{\beta} - A_+(x_{-+}-4)\left(\frac{x_{-+}}{A_+}\right)^{\beta}\right]$$
$$+\frac{B_m\kappa_c^{1-1/\beta}}{2^{1+1/\beta}\cdot 3^{1/\beta}}\left[(12-\xi x_{--})(x_{--}+2)^{1/\beta}\right.$$
$$-(12-\xi x_{+-})(x_{+-}+2)^{1/\beta} + (12-\xi x_{++})$$
$$\left.\times(x_{++}+2)^{1/\beta}(12-\xi x_{-+})(x_{-+}+2)^{1/\beta}\right]\Bigg\}$$

$$F_{\rm tot}^{(6)} = -\frac{2\pi m_0 R_s^2 \mathcal{L}_r}{\xi(\xi-2)}\left\{\frac{B_0\xi^2}{3\cdot 2^{2+\beta}}\left(\frac{B_m}{B_0}\right)^{\beta}\right.$$
$$\times\left[A_+(x_{++}-4)\left(\frac{x_{++}}{A_+}\right)^{\beta} - A_+(x_{-+}-4)\left(\frac{x_{-+}}{A_+}\right)^{\beta}\right]$$
$$+\frac{B_m\kappa_c^{1-1/\beta}}{2^{1+1/\beta}\cdot 3^{1/\beta}}\left[(12-x_{++}\xi)(x_{++}+2)^{1/\beta}\right.$$
$$\left.-(12-x_{-+}\xi)(x_{-+}+2)^{1/\beta}\right]\Bigg\}$$

$$F_{\rm tot}^{(7)} = 0$$

where the superscripts on $F_{\rm tot}$ correspond to the various regions shown in Fig. 4. Details are given in Appendix A.1.

### *2.3. Thin Spin Layer—Rectangular Line Shape*

The approximation of a rectangular line shape allows us to treat this problem analytically. We assume the sample consists of a thin layer of spins buried in an otherwise inert material as shown in Fig. 5. This might correspond to, e.g., a layer of $^{31}$P as thin as a few hundred nanometers ion implanted into silicon. We explore the relationship between the intrinsic line shape and

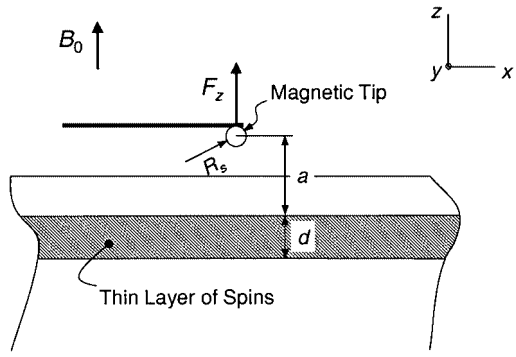


**FIG. 5.** Geometry for sample consisting of a thin layer of buried spins. Notation is as in Fig. 2. This is an important geometry since buried interfaces are often encountered in modern materials technologies. It also highlights a strength of the MRFM relative to other scanned probe techniques which are sensitive to surfaces only.

the mechanically detected spectrum $z(B_0)$. The lower boundary to the spatial spin distribution introduces a second boundary for the magnetic induction $B_d(x)$

$$B_d(x) = \left(\frac{\kappa_d}{\kappa_c}\right)^{-\xi/2} B_c(x) \qquad [25]$$
$$\kappa_d = \left(\frac{a+d}{R_s}\right)^2$$

so the region over which Eq. [22] is integrated is given by

$$x \in [-2, 4] \quad \text{and} \quad B \in [B_d(x),\, B_c(x)]$$

where $B_c(x)$ is given by Eq. [14].

With this additional boundary line there will be two sets of solutions ($\xi \gtrsim 2$) for the crossing points between $B_\pm(x)$ and $B_{c,d}(x)$ (see also Appendix A.5):

$$x_{\mp\pm}^{(c)} = -1 \mp \sqrt{1+\kappa_c\frac{12B_0A_\pm}{B_m}}$$
$$x_{\mp\pm}^{(d)} = -1 \mp \sqrt{1+\kappa_d\frac{12B_0A_\pm}{B_m}}$$

A typical situation for a particular value of the external magnetic induction $B_0$ is shown in Fig. 6. The area between the curves $B_c$ and $B_d$ corresponds to the spin layer, and the area between the curves $B_+$ and $B_-$ represents the sensitive slice, so the resonant force signal arises from the region defined by the intersection of these two sets of curves.

The structure of the resulting formulae for $F_{\rm tot}$ is similar to that for the semiinfinite sample, though there are a larger number of possible cases as a function of $B_0$; we present only the general

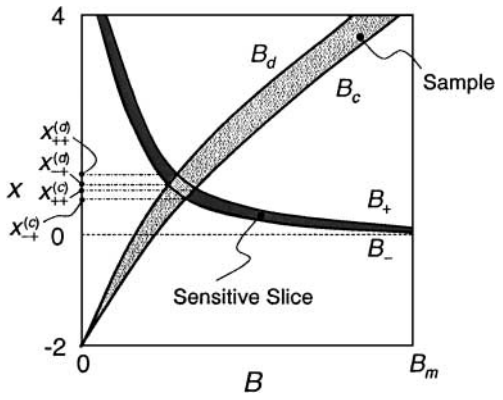


**FIG. 6.** Region of a buried spin layer meeting the resonance condition using the variable representation given in Eq. [12]: $x = 3\cos(2\theta) + 1$ and $B = B_m(R_s/r)^{\xi}$. In this representation the area between the curves $B_c$ and $B_d$ corresponds to the spin layer, and the area between the curves $B_+$ and $B_-$ represents the sensitive slice. The resonant force signal arises from the region bounded by these four curves.

expression for the resulting force:

$$F_{\text{tot}}^{(\alpha)} = C_0\left\{C_1\sum_{\{k_\alpha\}}(-1)^{k_0}A_{k_1}\left(x_{k_2k_1}^{(k_3)}-4\right)\left(\frac{x_{k_2k_1}^{(k_3)}}{A_{k_1}}\right)^{\beta} + C_2\sum_{\{j\alpha\}}(-1)^{j_0}\kappa_{j_3}^{1-\frac{1}{\beta}}\left(12-\xi x_{j_2j_1}^{(j_3)}\right)\left(x_{j_2j_1}^{(j_3)}+2\right)^{\frac{1}{\beta}}\right\}$$

where $\{k_\alpha\}$, $\{j_\alpha\}$ are sets of vectors involving $k_0 = 0, 1$, $k_{1,2} = +, -$ and $k_3 = c, d$ (analogously for the $j$'s). The $C$'s are given by

$$C_0 = -\frac{2\pi m_0 R_s^2 \mathcal{L}_r}{\xi(\xi-2)}$$

$$C_1 = \frac{B_0\xi^2}{3\cdot 2^{2+\beta}}\left(\frac{B_m}{B_0}\right)^{\beta}$$

$$C_2 = \frac{B_m}{2^{1+1/\beta}\cdot 3^{1/\beta}}$$

Detailed results are given in Appendix A.5, Eqs. A.6.

## 3. NUMERICAL SOLUTIONS

For the numerical analysis it is convenient to switch to cylindrical coordinates. The sample volume was broken into prisms constituting unit cells of calculation. The appropriate components of the magnetic field of the probe magnet and of its gradient were calculated at the center of each prism, and the instantaneous spin magnetization in each prism was also calculated taking into account the frequency and amplitude of the applied rf-field and the magnitude of the total magnetic induction $\boldsymbol{B}_{\text{tot}}$. All parameters are assumed constant over the volume of the prism. The cylindrical symmetry about $\boldsymbol{e}_z$ allows the evaluation of all necessary parameters only in the $rz$-plane. Thus, all samples are considered to be cylinders with radius $R$ and length $Z$.

The calculation time was reduced by employing an adaptive grid size (in the $rz$-plane) method. The size of the unit cell was determined by the requirement that it be $N$ times narrower than the thickness of the sensitive slice at the particular point in the sample. The thickness of the sensitive slice is given by the ratio of the magnetic resonance linewidth and the local gradient of magnetic field $\delta\omega(r,z)/|\nabla\omega_S(r,z)|$. We found $N = 2$ to be sufficient for the cases discussed here.

## 4. EXPERIMENT

The magnetic resonance force microscope apparatus is shown schematically in Fig. 7. A detailed description will be published elsewhere. The paramagnetic test sample consisted of 2,2-Di(4-tert-octylphenyl)-1-picrylhydrazyl (DPPH) powder (*26*) with a typical grain size of the order of 100 $\mu$m was fixed with vacuum grease to a slot in semirigid coaxial 50 Ω transmission line. A single crystal silicon cantilever with a length of 350 $\mu$m, a spring constant $k \simeq 0.01$ N/m and a typical resonance frequency of ≈16 kHz (*27*) was used to detect the force. The tip mounted on the end of the cantilever is coated with a 150 nm thick permalloy film; the tip radius then is approximately this same size.

The electron spins in the sample are polarized by an external magnetic induction $B_0$ and experience in addition the very inhomogeneous field of the micromagnet. The spins are resonantly excited by a microwave frequency field (9.9 GHz), which is either frequency- or amplitude-modulated at the frequency of the cantilever in order to generate a resonant force. The microwave-field is delivered to the sample by means of a 50 Ω transmission line as indicated in Fig. 7.

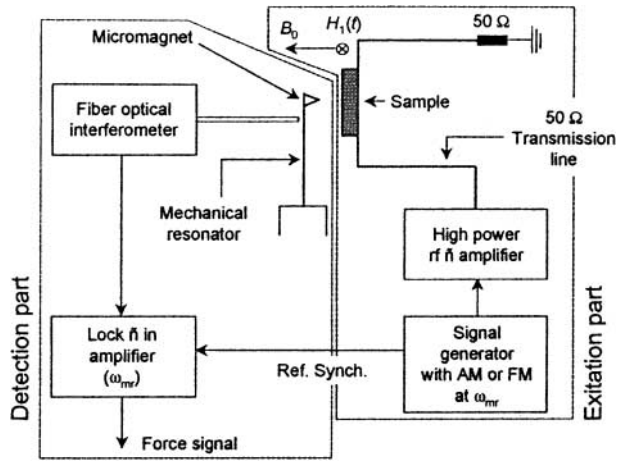


**FIG. 7.** Block diagram of the magnetic resonance force microscope. The signal excitation component resembles standard continuous wave magnetic resonance; detection is by means of mechanical resonator incorporating a micromagnetic tip and its associated displacement detection equipment.

## 5. DISCUSSION

The eventual goal of the MRFM is to achieve single spin sensitivity; this raises important questions such as that of continuous quantum measurement (*28, 29*). However, present sensitivity does not enable detection of only a very few spins and hence geometrical effects due to the coupling are of paramount importance as we will discuss in some depth here. Naïvely one would expect the strongly inhomogeneous magnetic field of the micromagnet to produce a broad resonant response as a function of the swept external field $B_0$ with a width set by the field distribution of the micromagnet. Our quantitative analysis shows that this does occur, however the magnitude of the displacement response of the mechanical resonator varies strongly with $B_0$ and hence this expected broadening can easily be hidden in a real experiment, due to noise or other limitations. The dominant response is found to occur for fields $B_0 \simeq \omega_{\rm rf}/\gamma$ (i.e., where the magnetic field of the micromagnetic probe is very small, that is, less than the linewidth); this response can be orders of magnitude more intense than any other resonant response. For $B_0 < \omega_{\rm rf}/\gamma$ the sensitive slice is a thin shell of constant field, however for $B_0 \simeq \omega_{\rm rf}/\gamma$ both the field and the field gradient of the micromagnet are very weak causing quite a large volume of the sample to be in resonance. This leads to a large signal in spite of the weak coupling per spin. In this case the concept of the sensitive slice must be extended. Furthermore, the sensitive slice and the local force field are related but not synonymous, and geometrical coupling effects can have important effects. Keeping these issues in mind, we will structure the discussion as follows: The findings of the analytical calculations will be discussed and then more realistic physical parameters will be discussed based on the numerical results. Finally, our findings will be compared with experimental results. Unless otherwise noted, the figures shown below are calculated using the parameters in Table 1.

Figures 8 and 9 show the magnitude of the displacement vs. the external applied magnetic induction $B_0$ as one would measure in a typical field-swept experiment. Both figures are for samples whose overall dimensions are much larger than the micromagnet. Figure 8 is calculated from Eq. [19] whereas Figure 9 is derived from Eq. [22].

**TABLE 1**

| | | |
|---|---|---|
| Relaxation times | $T_1 = T_2$ | 60 ns |
| Mechanical resonator resonance frequency | $\omega_{\rm mr}$ | $2\pi \cdot 10$ kHz |
| Field at the surface of the micromagent | $B_m$ | $\frac{4\pi}{3} \cdot 860$ G |
| Spatial variation of probe field (Eq. [5]) | $\xi$ | 2.005 |
| Rf-field frequency | $\omega_{\rm rf}/\gamma$ | 1 T |
| Rf-field amplitude | $H_1$ | 1 G |
| Rf-field modulation (Eq. [17]) | $\zeta$ | 1 |

*Note.* Unless otherwise noted, the following parameters were used for the calculations presented here. These parameters correspond to EPR either in DPPH, or in phosphorus implanted silicon at a doping level of $8 \times 10^{17}$ cm$^{-3}$, both at $T = 4$ K.

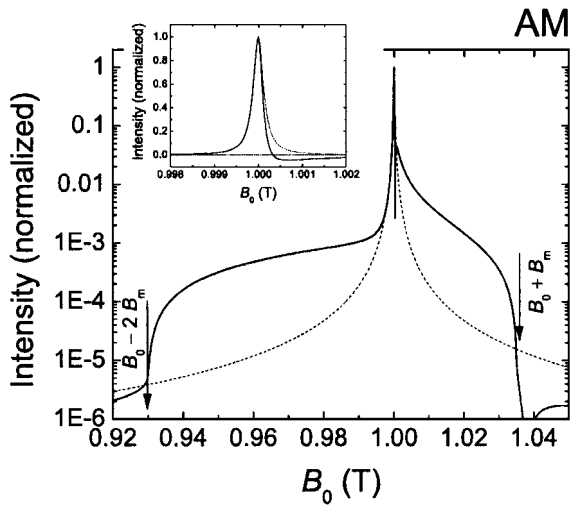


**FIG. 8.** Response of a mechanical resonator vs $B_0$ for amplitude modulation (AM) in the case of a Lorentzian line shape and an extended semi-infinite sample as calculated in Section 2.1 ($\xi = 2$, $B_m = 350$ $G$). The dashed line shows the intrinsic line shape one would measure in a standard EPR experiment. The inset is a blow-up of the center of the resonance, with intensity plotted on a linear scale.

One finds a very strong response for $B_0 = \omega_{\rm rf}/\gamma$. Since this feature will occur in later discussions we introduce the term "zero-probe-field resonance" (ZPFR), referring to the situation $B_0 = \omega_{\rm rf}/\gamma$. In this case broadening due to the field distribution of the micromagnet is present, however it is much smaller than in regions where the probe field is larger, that is where $B_0$ deviates from the ZPFR-value ($\omega_0 \gtrless \omega_{\rm rf} \pm \delta\omega$). In the highly symmetric case shown in Fig. 8 (Lorentzian line shape with micromagnet

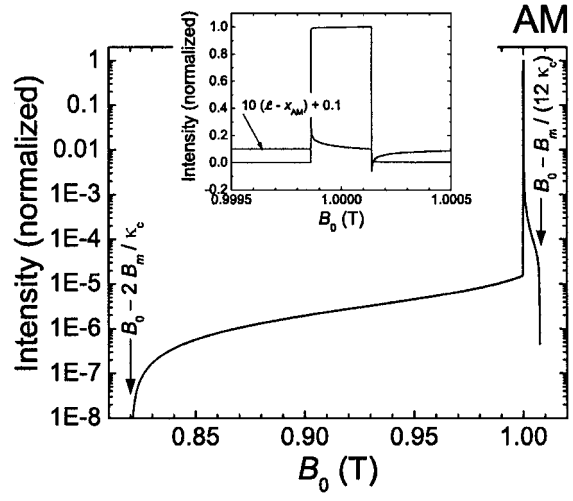


**FIG. 9.** Response of a mechanical resonator vs $B_0$ for AM in the case of a rectangular line shape and an extended semi-infinite sample as calculated in Section 2.2. $R_s : a = 1 : 2$. Notice that the response is similar to the Lorentzian case in Fig. 8. The one clear difference, the much reduced extent of the high field shoulder, is due to the fact that the micromagnet has been raised above the sample surface, thus reducing the coupling range ($\theta$ is always greater than $\pi/2$).

embedded in the sample surface as shown in Fig. 3) the full broadening expected due to the dipole field of the micromagnet is found as indicated by the arrows in the figure. Here $\xi = 2$ and $B_m$ is set to 350 G to satisfy the constraint that the local field of the micromagnet in the sample be much smaller than the external field.

The response for the case of the rectangular line shape is similar as can be seen from Fig. 9. Here the micromagnet is positioned above the sample ($R_s : a = 1 : 2$, see also Fig. 2). Because the probe has been raised, the high field shoulder is much less extended. To understand these features better, we consider the concept of the sensitive slice and show that for some values of $\omega_0$ it differs from that usually discussed (5). The sensitive slice is defined as the resonant region of the sample. Since the micromagnet leads to a strong inhomogeneous magnetic induction in its vicinity only part of the sample will resonate. An estimate of the spatial width of the sensitive slice is $x_{\mathrm{s1}} \approx \delta\omega/\nabla\omega_S$, where $\delta\omega$ is the intrinsic homogeneous line width and $\omega_S$ is given by Eq. 7. This expression is similar to the one used in conventional MRI. However, due to the large variation in the gradient of the magnetic induction of the micromagnet this simple concept must be taken with some caution. For fields $\omega_0 \lesssim \omega_{\mathrm{rf}}$ the sesnsitive slice is a constant-field shell whose width is indeed approximately $x_{\mathrm{sl}}$. This situation, shown in Figs. 10a and 10b is the situation usually considered in the context of the MRFM. The right-hand side of Fig. 10 shows the resonant magnetization, whereas the left-hand side shows the local coupling force strength weighted by the volume of the sample exhibiting this force; we will call this the force slice. Between (a) and (b) the external field $B_0$ is increasing resulting in a more extended sensitive slice $x_{\mathrm{sl}}$ since the gradient $\nabla\omega_S$ is decreasing.

It is also worth noting that the force slice shows a sign change (green corresponds to negative force coupling, or a force whose phase is shifted by 180° with respect to the excitation signal, whereas red–yellow corresponds to positive, or in-phase, force coupling). The purple line in Fig. 10 separates the regions of positive and negative force coupling.

There are two additional cases to consider: (i) the ZPFR where $\omega_{\mathrm{rf}} - \delta\omega \leq \omega_0 \leq \omega_{\mathrm{rf}} + \delta\omega$. In this situation, due to the finite magnetic resonance line width and the very small field gradient in this region of small field, the entire sample is in resonance except for regions very close to the micromagnet where the magnitude of the local field is too large. This is shown in Fig. 10c. In this situation $x_{\mathrm{sl}}$ is not a meaningful length scale since $x_{\mathrm{sl}}$ changes very rapidly as function of position. (ii) $\omega_0 \gtrsim \omega_{\mathrm{rf}}$. Here one finds a toroidal sensitive slice as shown in Fig. 10d with a width of order $x_{\mathrm{sl}}$. We will focus on samples with overall spatial dimensions much larger than the micromagnet (i.e., $\gtrsim R_s = 150$ nm in our case) discussing other situations later on. The field-swept response shown in Figs. 8 and 9 shows that the strongest signal originates in the field range $\omega_0 \approx \omega_{\mathrm{rf}}$, i.e., the situation where a large sample volume is resonant. For homogeneously broadened lines (where there is a simple mapping between spectral and spatial dimensions) the low field shoulder of the ZPFR accurately reproduces the intrinsic spectrum as can be seen from Figs. 8 and 9. In this low sensitivity regime valuable parameters like the chemical shift can be directly read off of the spectrum, since the shift and broadening of the line by the probe micromagnet is very small. However, since a large volume of sample is in resonance this information is not obtained from a particularly

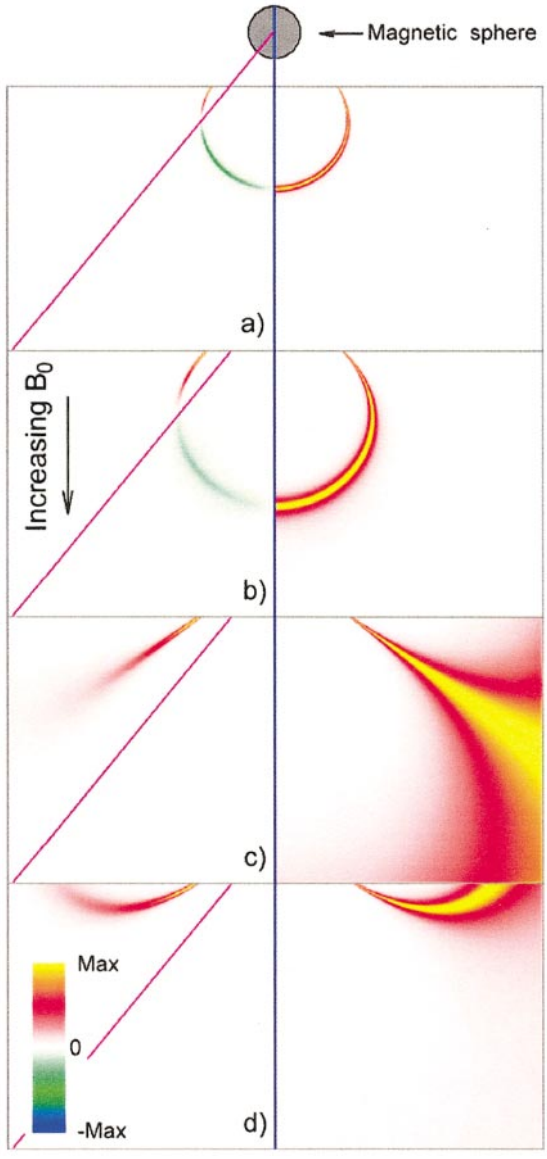


**FIG. 10.** Calculation of the sensitive slice shape (right hand panels) and force slice (left hand panels) for different external field values $B_0$. The force slice is weighted by the volume element. The purple line on the left (force slices) marks the angle at which the local force changes sign (see also Fig. 2): (a) ($B_0 = 0.9965\ T$) and (b) ($B_0 = 0.9985\ T$) show typical sensitive slices as shells of constant field for $\gamma B_0 < \omega_{\mathrm{rf}}$; (c) shows the situation for $\gamma B_0 = \omega_{\mathrm{rf}}$. Since the gradient is very small in the regions where the resonance condition is met the ratio of the line width to the gradient is very large, hence a large volume of sample meets the resonance condition. The conventional concept of a typical length scale $x_{\mathrm{sl}} \approx \delta\omega/\nabla\omega_s$ breaks down in this case. (d) $\gamma B_0 > \omega_{\mathrm{rf}}$ ($B_0 = 1.0005\ T$). Here the shape of the sensitive is approximately toroidal.

microscopic spatial region. The region of the sample contributing substantially to the resonant signal is of the order 100 $R_s$.

From this discussion it is also clear that the ZPFR will not depend strongly on the distance separating the micromagnet and the surface. The only effect is a gradual decrease of the signal size. This is shown in Fig. 12. Instead, it is the low and high-field shoulders of the spectrum that are ($\omega_0 \gtrless \omega_{\rm rf} \pm \delta\omega$) strongly influenced.

It is useful to study how the signal is influenced by structures whose dimensions are comparable to the size of the micromagnet. In Section 2.3 (see also Appendix A.5) we calculate the force field stemming from a thin magnetic layer with a thickness comparable to the size of the micromagnet. The geometry used is presented in Fig. 5. Figure 11 shows the field-swept response in the case of a signal excited by amplitude modulation. The field-swept spectrum is quite different from that produced by the semiinfinite sample discussed above. The ZPFR line previously found at resonance is replaced by a sharp

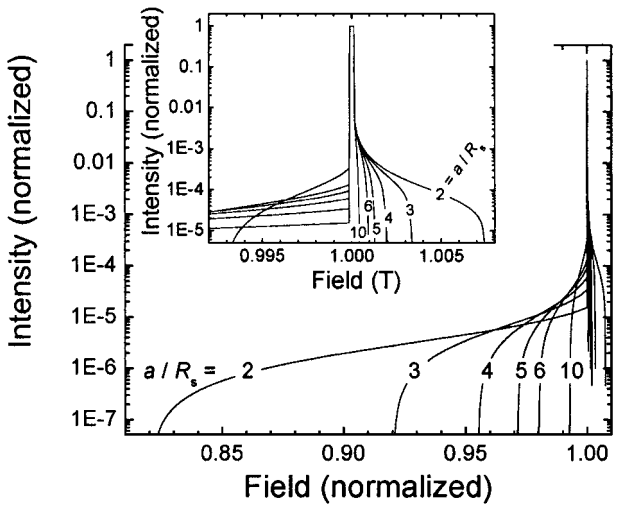


**FIG. 12.** Semiinfinite sample spectra for various micromagnet-sample separations. The primary effect of moving the micromagnet away from the surface (increasing $a/R_s$) is a reduction in the extent of the low- and high-field shoulders.

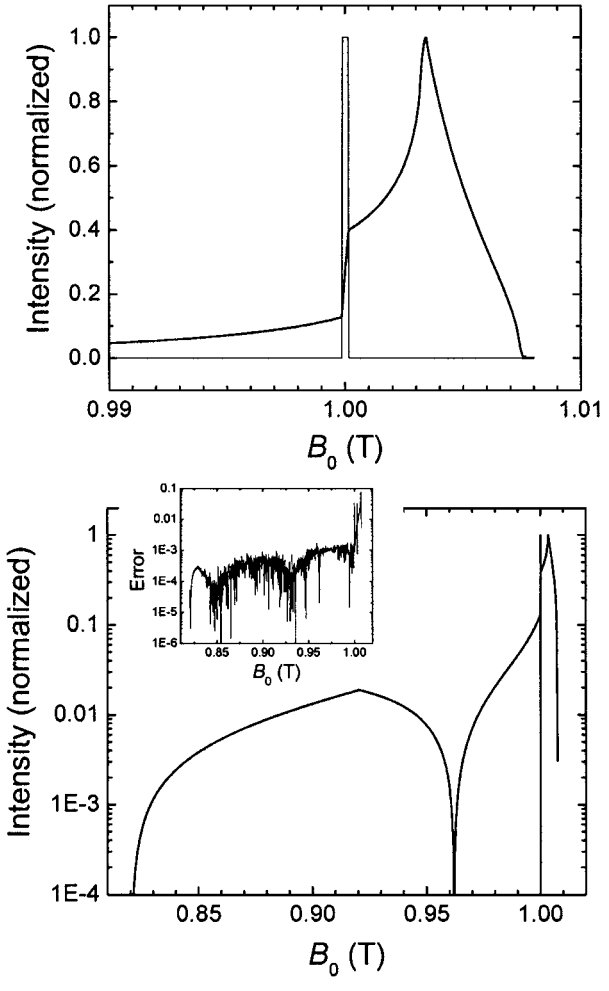


**FIG. 11.** Response of the mechanical resonator vs $B_0$ using AM for a thin buried layer as described in Section 2.3 and Fig. 5. The thin sharp line at $B_0 = 1\ T$ shows the intrinsic line. $R_s : a : d = 1 : 2 : 1$. The inset shows the discrepancy between the analytical and numerical solution.

edge to the strong response whose peak appears at higher field. This pronounced peak is shifted by approximately 35 G relative to the intrinsic resonance for our chosen parameters. The peak position is an indirect measure of the thickness of the spin-layer; unfortunately it is difficult to derive an analytical expression for the relation between thickness and the peak position. Qualitatively one finds that they are reciprocal, i.e., as the layer becomes thicker, the peak is shifted closer to the ZPFR.

On the low field side the force changes sign for the reasons we have discussed (see Fig. 2). The sign change occurs near a field of 0.962 T; the angle at which the local $F_z$-force coupling is zero is given by Eq. [10]. At very low fields the onion-shell like sensitive slice is entirely within the negative force coupling region. With increasing field portions of the sensitive slice enter the positive-force region and at some point (for the parameters we consider) there is a cancellation.

The inset to Fig. 11 shows the difference between the analytical and numerical solutions $|z_{\rm analytic}(B_0) - z_{\rm numerical}(B_0)|$. This deviation is of order 1%, except for the high field region ($B_0 > \omega_{\rm rf}/\gamma$) where it becomes larger. In this region the analytical solution involves an approximation for the point at which the sensitive slice enters the sample; this leads to tangents between the surface of the sample and the sensitive slice with very small differences and therefore to small systematic deviations. Using the more realistic Lorentzian lineshape in place of the rectangular in the numerical approach we find that the field-swept spectrum in Fig. 11 is changed in amplitude but its shape is unchanged (not shown here). The difference in amplitude is $\pi/2$, the difference between the integrals of rectangular and Lorentzian line shapes.

For the thin layer sample ($R_s : a : d = 1 : 2 : 1$, Fig. 5) we numerically calculated the AM-response for more realistic parameters $\xi = 3$ and a Lorentzian line shape. The other parameters are as given in Table 1. The result is shown in Fig. 13. As one can

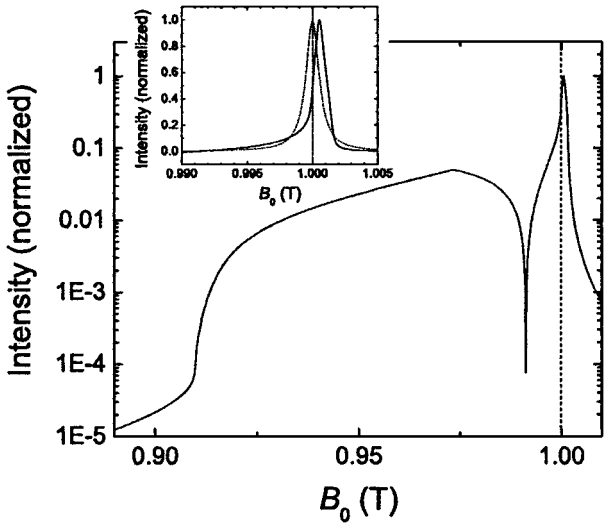


**FIG. 13.** Response of the mechanical resonator vs $B_0$ using AM for a thin buried layer as described in Section 2.3. The thin sharp line at $B_0 = 1\ T$ shows the intrinsic line. The response is calculated numerically for the same parameters as shown in Fig. 11 ($R_s : a : d = 1 : 2 : 1$), except that a Lorentzian line shape and a more realistic $\xi = 3$ was used. The inset shows the region close to the ZPFR on a linear scale. The dashed curve represents the intrinsic EPR-line shape.

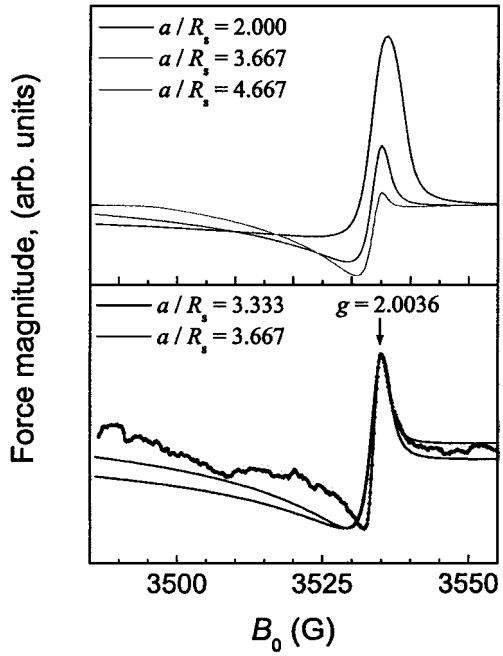


**FIG. 14.** Bottom panel: Filled circles represent the signal from 2,2-Di(4-tert-octylphenyl)-1-picrylhydrazyl (DPPH) powder at $T = 4$ K. The response was obtained by amplitude modulation at a rf-frequency of $\omega_{\rm rf} = 2\pi \cdot 9.9$ GHz. The colored curves show the response calculated from our model for specific values of $a/R_s$. The experimental measurements were performed on a powder sample, so we assume coupling to a single grain. We approximate the grain geometry as a cylinder whose diameter is $20\,R_s$, and height is $10\,R_s$. The top panel shows the calculated evolution of the signal with increasing $a/R_s$.

see, the general character is not altered. Due to the Lorentzian line shape all the features are broadened, as one would expect. The more rapid drop off of the field of the micromagnet ($\xi = 3$) causes all the observable features to fall in a narrower range of field $B_0$.

Comparison of these results show that the general features are rather robust under variation of the parameters describing the micromagnet and lineshape, so the solutions presented here provide a general and reliable guide to further analysis.

We now provide a brief comparison with experimental data. A typical field scan using amplitude modulation is shown in Fig. 14. This spectrum appears to be a mixture between the calculation for a semiinfinite sample (Fig. 8) and a thin-layer sample (Fig. 13). We attribute this to the fact that the DPPH powder sample is made up of crystallites of various sizes. The distinctive features are present however, including the peak at ZPFR ($g = 2.0036$) and the negative response below the resonance field. Experiments that will provide quantitative comparison with the calculations are underway.

## 6. SUMMARY

We have presented a detailed analysis of the interactions which underlie the functionality of the magnetic resonance force microscope (MRFM) for the important situation where a micromagnetic probe mounted on the force detector detects the signal from an extended sample—the case encountered with a general scanning probe microscope. In particular we have focused on the implications of having at least one dimension of the sample much larger than the micromagnet.

We have shown that in addition to the concept of a sensitive slice (the spatial region where the magnetic resonance condition is fulfilled) one should consider the concept of a force slice (volume of the sample that exerts force on the mechanical resonator due to magnetic resonance manipulation of the magnetization). This distinction is important because of the dipolar nature of probe magnetic field which causes the magnitude and even the sign of the force to vary throughout the force slice. (A negative force means a 180° phase shift of the time-dependent force with respect to the excitation signal.) Since the total driving force is the integral over the entire force slice, this leads to cancellation of forces, and for certain values of $B_0$ the total driving force is zero. This is notable given that we nonetheless have a well-defined resonant sensitive slice.

We find that in a typical field-swept experiment the concept of the sensitive slice must be taken with caution: (i) For fields $\omega_0 < \omega_{\rm rf} - \delta\omega$ ($\omega_0 = \gamma B_0$ with $B_0$ the external magnetic induction, $\omega_{\rm rf}$ the rf-frequency and $\delta\omega$ the homogeneous intrinsic line width) the form of the sensitive slice resembles an ellipsoidal shell, and the idea of a typical length scale $x_{\rm sl} \approx \delta\omega/(\gamma \nabla B)$ is useful. This situation is widely discussed in the literature. (ii) $|\omega_0 - \omega_{\rm rf}| < \delta\omega$: In this field regime virtually the entire sample is in resonance except for regions very close the micromagnet where its large positive (below the magnet) or negative (to the

side) field shifts spins out of resonance. Obviously in this situation the concept of a typical length scale is questionable. Due to the rapid decrease of the gradient of the micromagnet, one can estimate that portions of the sample separated from the micromagnet by less than approximately 100 times the radius of the micromagnet will contribute to the force signal. Thus, the total force stemming from this field regime is quite large if the overall dimensions of the sample are much larger than the micromagnet. This contribution will lead to the dominant peak in the field-swept spectrum and can obscure the expected broadening due to the inhomogeneous field of the micromagnet. (iii) $\omega_0 > \omega_{\rm rf} - \delta\omega$: The sensitive slice is a toroid-like structure to the side of the micromagnet; here the concept of a typical length scale $x_{\rm sl}$ recovers.

The practical importance of these phenomena for scanned probe experiments has been shown in experiments employing DPPH powder samples having typical grain size of the order of tens of microns. These spectra exhibit the change in sign of the driving force field, and the cancellation of the total force for a specific value of $B_0$ discussed above.

## APPENDIX

### *A.1. Rectangular Line Shape, Semi-infinite Sample, $\omega_m/(12\kappa_c) > 2\delta\omega$*

We will discuss the solution of Eq. [13] in $(x, B)$-parameter space (see Eq. [12] for definitions of $x$ and $B$). The resonant region of the sample is bounded by three curves. The first is $B_c(x)$ which is determined by the location of the sample surface; the region above and to the left of $B_c(x)$ is occupied by sample, while below and to the right is empty space above the sample surface. The other two curves $B_\pm(x)$ are boundaries of the resonant region determined by the rectangular line shape. For convenience we give these equations, even though some have appeared earlier.

$$B_c(x) = B_m\left(\frac{x+2}{6\kappa_c}\right)^{\xi/2} \qquad [A.1]$$

$$B_\pm(x) = \frac{2B_0A_\pm}{x} \qquad [A.2]$$

In the following we will move freely between angular frequency notation and field notation; throughout $\omega_\alpha = \gamma B_\alpha$. We only take resonant regions into consideration and $F_{\rm tot}(t)$ does not include time-dependent forces since we are only interested in spectral weight around $\omega_{\rm mr}$.

The relevant external parameter in the problem is $\omega_0$. The volumes bounded by $B_c(x)$ and $B_\pm(x)$ define resonant parts of phase space; to define these boundaries we require the points at which $B_c(x)$ and $B_\pm(x)$ cross, this is given by:

$$B_m\left(\frac{x+2}{6\kappa_c}\right)^{\xi/2} = \frac{2B_0A_\pm}{x}$$

In the interest of simplicity we set $\xi = 2$ as an approximation. Then

$$x_{\mp\pm} = -1 \mp \sqrt{1 + \kappa_c\frac{12B_0A_\pm}{B_m}}$$

i.e.,

$$x_{+-} = -1 + \sqrt{1 + \kappa_c\frac{12B_0A_-}{B_m}}.$$

The restriction to real solutions gives

$$\omega_0 \le \omega_{\rm rf} \pm \delta\omega + \frac{\omega_m}{12\kappa_c}$$

where $\delta\omega = 1/T_2\sqrt{1+\omega_1^2T_1T_2}$. The second restriction enters through the requirement that the crossing point must be within the parameter space, especially that $x_{\mp\pm} \le 4$. This yields

$$\omega_0 \ge \omega_{\rm rf} \pm \delta\omega - 2\omega_m/\kappa_c$$

The evolution of this resonant volume with $B_0$ depends on experimental parameters; this evolution is depicted in Fig. 4 for the case $\omega_m/(12\kappa_c) > 2\delta\omega$ (which arises typically when the separation between the micromagnet and the sample surface is comparable to the size of the micromagnet). It is instructive to sketch this situation graphically as shown in Fig. A1.

### *A.2. Rectangular Line Shape, Semi-infinite Sample, $\omega_m/(12\kappa_c) < 2\delta\omega < 2\omega_m/\kappa_c$*

The solution is similar to Eq. [24] except the ranges of validity are given as in Fig. A2, and $F_{\rm tot}^{(5)}$ is changed:

$$F_{\rm tot}^{(5)} = -\frac{2\pi m_0R_s^2\mathcal{L}_r}{\xi(\xi-2)}\left[\frac{B_0\xi^2}{3\cdot 2^{1+\beta}}A_+(x_{++}-4)\left(\frac{B_mx_{++}}{B_0A_+}\right)^\beta + \frac{(6\kappa_c)^{1-1/\beta}}{12}B_m(12-\xi x_{++})(x_{++}+2)^{1/\beta}\right]. \qquad [A.3]$$

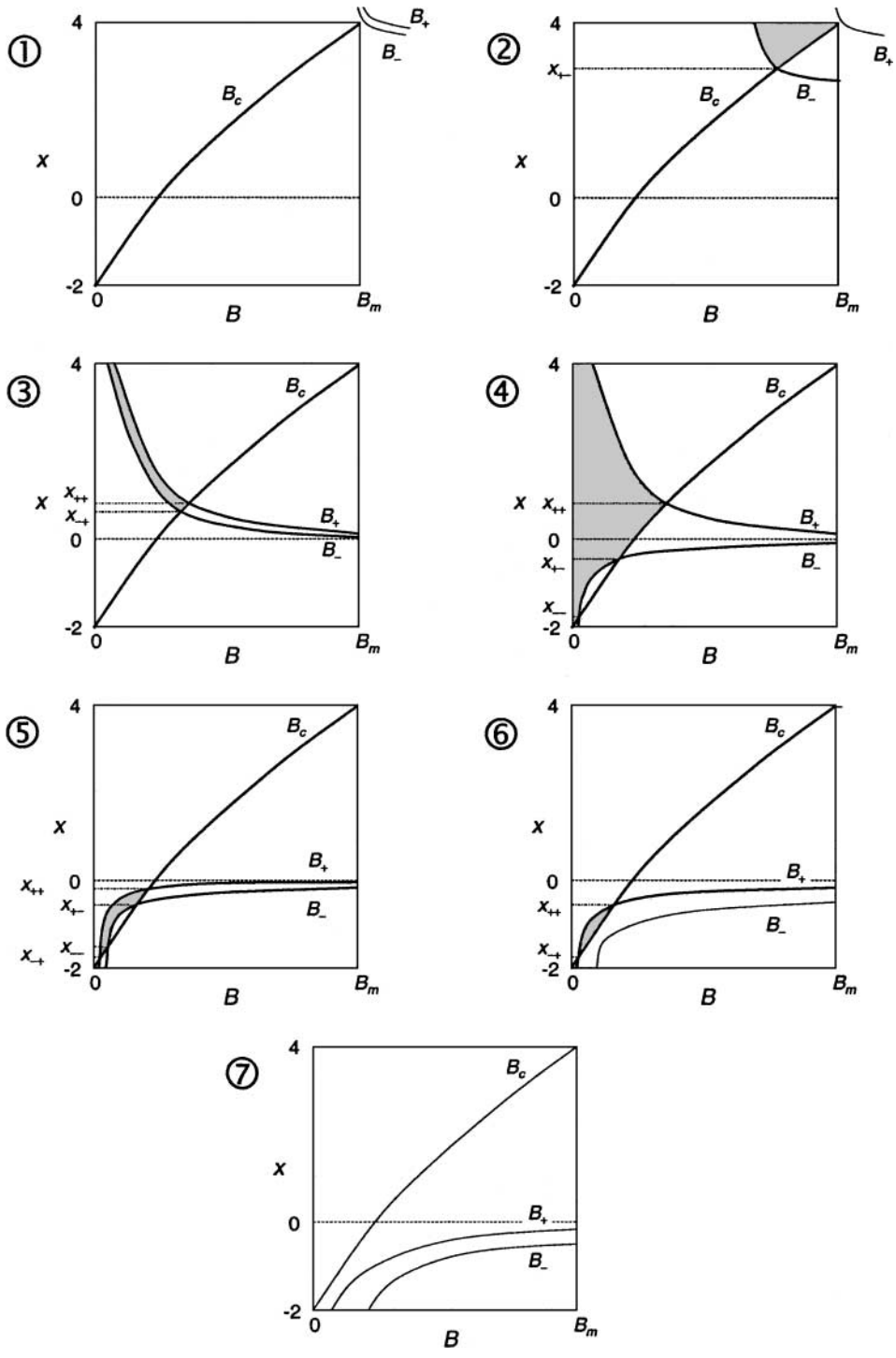


**FIG. A1.** Resonant region in $(B, x)$-space vs $B_0$ for the case of a semi-infinite sample with $\omega_m/(12\kappa_c) > 2\delta\omega$. The situations 1–3 correspond to an onion-shell-like sensitive slice (SSL). In 4 virtually the entire sample is in resonance, 5–7 corresponds to an approximately toroidally shaped sensitive slice to the side of the micromagnet. 1: The external field is too small, hence the SSL is above the sample. 2: The SSL just enters the top surface of the sample. 3: The entire width of the SSL has penetrated into the sample. 4: Most of the sample resonates. 5: The SSL forms a toroidally shaped structure. 6: The SSL partially leaves the sample. 7: $B_0$ is too large and the SSL is again above the sample to the side. See also Fig. 10.

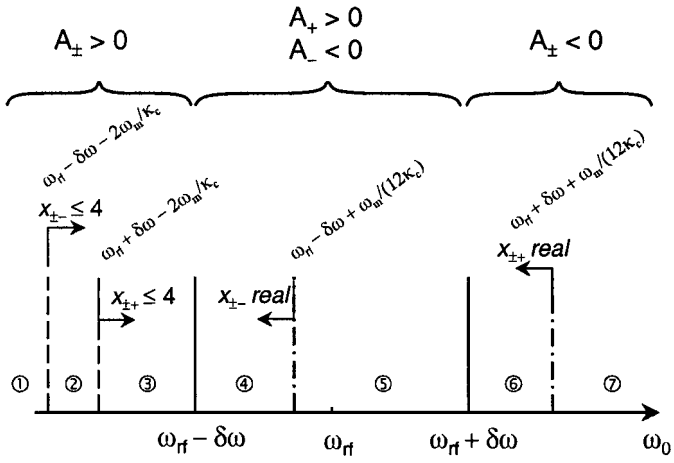


**FIG. A2.** Regions of phase space vs $\omega_0$ for $\omega_m/(12\kappa_c) < 2\delta\omega < 2\omega_m/\kappa_c$.

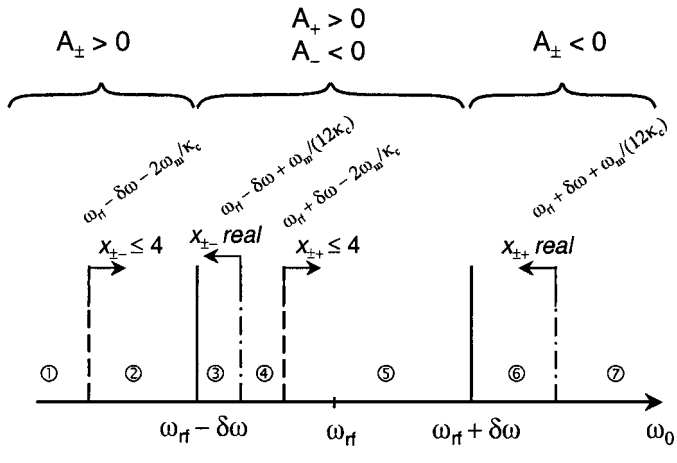


**FIG. A4.** Regions of $(B, x)$-space vs $\omega_0$ for $2\delta\omega > (2\omega_m + \omega_m/12)/\kappa_c$.

### *A.3. Rectangular Line Shape, Semi-infinite Sample, $2\omega_m/\kappa_c < 2\delta\omega < (2\omega_m + \omega_m/12)/\kappa_c$*

The solution is similar to Eq. [24], except the ranges of validity are as shown in Fig. A3 and $F_{\text{tot}}^{(3,5)}$ are given by

$$F_{\text{tot}}^{(3)} = \frac{2\pi m_0 R_s^2 \mathcal{L}_r}{\xi(\xi-2)}\left\{2B_m(3-\xi) + \frac{B_0\xi^2}{3\cdot 2^{2+\beta}}\left(\frac{B_m}{B_0}\right)^{\beta}\right.$$
$$\times\left[A_-(x_{--}-4)\left(\frac{x_{--}}{A_-}\right)^{\beta} - A_-(x_{+-}-4)\left(\frac{x_{+-}}{A_-}\right)^{\beta}\right]$$
$$-\frac{B_m\kappa_c^{1-1/\beta}}{2^{1+1/\beta}\cdot 3^{1/\beta}}\left[(12-\xi x_{+-})(x_{+-}+2)^{1/\beta}\right.$$
$$\left.\left.-(12-\xi x_{--})(x_{--}+2)^{1/\beta}\right]\right\} \qquad \text{[A.4]}$$

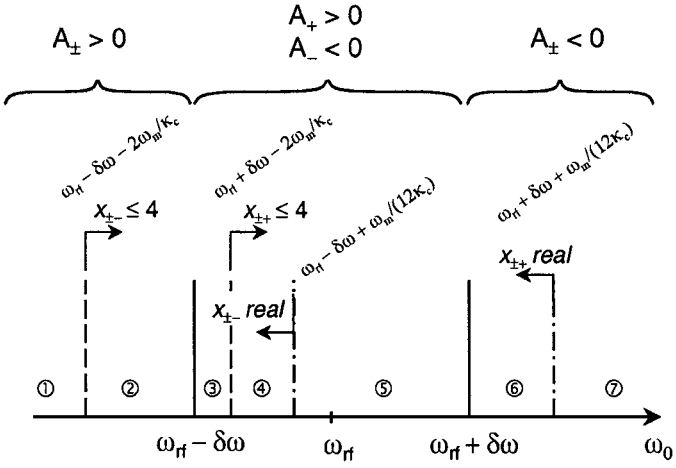


**FIG. A3.** Separation of the phase space vs $\omega_0$ for $2\omega_m/\kappa_c < 2\delta\omega < (2\omega_m + \omega_m/12)/\kappa_c$.

$$F_{\text{tot}}^{(5)} = -\frac{2\pi m_0 R_s^2 \mathcal{L}_r}{\xi(\xi-2)}\left[\frac{B_0\xi^2}{3\cdot 2^{1+\beta}}A_+(x_{++}-4)\left(\frac{B_m x_{++}}{B_0 A_+}\right)^{\beta}\right.$$
$$\left.+\frac{(6\kappa_c)^{1-1/\beta}}{12}B_m(12-\xi x_{++})(x_{++}+2)^{1/\beta}\right].$$

### *A.4. Rectangular Line Shape, Semi-infinite Sample, $2\delta\omega > (2\omega_m + \omega_m/12)/\kappa_c$*

The solution is similar to Eq. [24], except the ranges of validity are as shown in Fig. A4 and $F_{\text{tot}}^{(3,4,5)}$ are given by

$$F_{\text{tot}}^{(3)} = \frac{2\pi m_0 R_s^2 \mathcal{L}_r}{\xi(\xi-2)}\left\{2B_m(3-\xi) + \frac{B_0\xi^2}{3\cdot 2^{2+\beta}}\left(\frac{B_m}{B_0}\right)^{\beta}\right.$$
$$\times\left[A_-(x_{--}-4)\left(\frac{x_{--}}{A_-}\right)^{\beta} - A_-(x_{+-}-4)\left(\frac{x_{+-}}{A_-}\right)^{\beta}\right]$$
$$-\frac{B_m\kappa_c^{1-1/\beta}}{2^{1+1/\beta}\cdot 3^{1/\beta}}\left[(12-\xi x_{+-})(x_{+-}+2)^{1/\beta}\right.$$
$$\left.\left.-(12-\xi x_{--})(x_{--}+2)^{1/\beta}\right]\right\} \qquad \text{[A.5]}$$

$$F_{\text{tot}}^{(4)} = -\frac{2\pi m_0 R_s^2 \mathcal{L}_r}{\xi(\xi-2)}2(\xi-3)\kappa_c^{1-1/\beta}$$

$$F_{\text{tot}}^{(5)} = -\frac{2\pi m_0 R_s^2 \mathcal{L}_r}{\xi(\xi-2)}\left[\frac{B_0\xi^2}{3\cdot 2^{1+\beta}}A_+(x_{++}-4)\left(\frac{B_m x_{++}}{B_0 A_+}\right)^{\beta}\right.$$
$$\left.+\frac{(6\kappa_c)^{1-1/\beta}}{12}B_m(12-\xi x_{++})(x_{++}+2)^{1/\beta}\right].$$

### *A.5. Thin Spin-Layer*

$$F_{\text{tot}}^{(1)} = 0$$

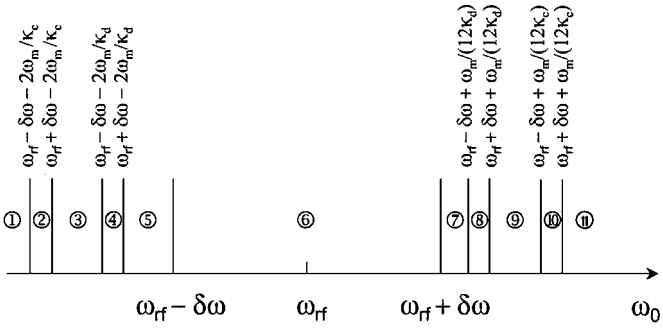


**FIG. A5.** Regions of $(B, x)$-space vs $\omega_0$ for the case of a thin layer of spins. $\omega_m/(12\kappa_d) > 2\delta\omega$.

$$F_{\text{tot}}^{(2)} = -\frac{2\pi m_0 R_s^2 \mathcal{L}_r}{\xi(\xi-2)}\left\{-\frac{B_0\xi^2}{3\cdot 2^{2+\beta}}\left(\frac{B_m}{B_0}\right)^{\beta}\right.$$
$$\times A_-\left(x_{+-}^{(c)}-4\right)\left(\frac{x_{+-}^{(c)}}{A_-}\right)^{\beta} + B_m\kappa_c^{1-1/\beta}$$
$$\left.\times\left[6-2\xi-\frac{\left(12-\xi x_{+-}^{(c)}\right)\left(x_{+-}^{(c)}+2\right)^{1/\beta}}{2^{1+1/\beta}\cdot 3^{1/\beta}}\right]\right\}$$

$$F_{\text{tot}}^{(3)} = -\frac{2\pi m_0 R_s^2 \mathcal{L}_r}{\xi(\xi-2)}\left\{\frac{B_0\xi^2}{3\cdot 2^{2+\beta}}\left(\frac{B_m}{B_0}\right)^{\beta}\right.$$
$$\times\left[A_+\left(x_{++}^{(c)}-4\right)\left(\frac{x_{++}^{(c)}}{A_+}\right)^{\beta} - A_-\left(x_{+-}^{(c)}-4\right)\left(\frac{x_{+-}^{(c)}}{A_-}\right)^{\beta}\right]$$
$$+\frac{B_m\kappa_c^{1-1/\beta}}{2^{1+1/\beta}\cdot 3^{1/\beta}}\left[\left(12-\xi x_{++}^{(c)}\right)\left(2+x_{++}^{(c)}\right)^{1/\beta}\right.$$
$$\left.\left.-\left(12-\xi x_{+-}^{(c)}\right)\left(2+x_{+-}^{(c)}\right)^{1/\beta}\right]\right\}$$

$$F_{\text{tot}}^{(4)} = -\frac{2\pi m_0 R_s^2 \mathcal{L}_r}{\xi(\xi-2)}\left\{\frac{B_0\xi^2}{3\cdot 2^{2+\beta}}\left(\frac{B_m}{B_0}\right)^{\beta}\left[A_-\left(x_{+-}^{(d)}-4\right)\left(\frac{x_{+-}^{(d)}}{A_-}\right)^{\beta}\right.\right.$$
$$+A_+\left(x_{++}^{(c)}-4\right)\left(\frac{x_{++}^{(c)}}{A_+}\right)^{\beta} - A_-\left(x_{+-}^{(c)}-4\right)\left(\frac{x_{+-}^{(c)}}{A_-}\right)^{\beta}\Big]$$
$$+\frac{B_m\kappa_c^{1-1/\beta}}{2^{1+1/\beta}\cdot 3^{1/\beta}}\left[\left(2+x_{+-}^{(c)}\right)^{1/\beta-1}\left(2x_{+-}^{(c)}\right)(\xi-6)+\xi\left(x_{+-}^{(c)}\right)^2\right.$$
$$\left.-24\right)+\left(2+x_{++}^{(c)}\right)^{1/\beta}\left(12-\xi x_{++}^{(c)}\right)\Big] + \frac{B_m\kappa_d^{1-1/\beta}}{2^{1+1/\beta}\cdot 3^{1/\beta}}$$
$$\left.\times\left[\left(2+x_{+-}^{(d)}\right)^{1/\beta}\left(12-\xi x_{+-}^{(d)}\right)+2\cdot 6^{1/\beta}(\xi-3)\right]\right\}$$

$$F_{\text{tot}}^{(5)} = -\frac{2\pi m_0 R_s^2 \mathcal{L}_r}{\xi(2-\xi)}\left\{\frac{B_0\xi^2}{3\cdot 2^{2+\beta}}\left(\frac{B_m}{B_0}\right)^{\beta}\left[A_+\left(x_{++}^{(c)}-4\right)\left(\frac{x_{++}^{(c)}}{A_+}\right)^{\beta}\right.\right.$$
$$-A_-\left(x_{+-}^{(c)}-4\right)\left(\frac{x_{+-}^{(c)}}{A_-}\right)^{\beta} + A_-\left(x_{+-}^{(d)}-4\right)\left(\frac{x_{+-}^{(d)}}{A_-}\right)^{\beta}$$
$$\left.\left.-A_+\left(x_{++}^{(d)}-4\right)\left(\frac{x_{++}^{(d)}}{A_+}\right)^{\beta}\right] + \frac{B_m\kappa_c^{1-1/\beta}}{2^{1+1/\beta}\cdot 3^{1/\beta}}\left[\left(12-\xi x_{++}^{(c)}\right)\right.\right.$$
$$\times\left(x_{++}^{(c)}+2\right)^{1/\beta} - \left(12-\xi x_{+-}^{(c)}\right)\left(x_{+-}^{(c)}+2\right)^{1/\beta}\Big]$$
$$+\frac{B_m\kappa_d^{1-1/\beta}}{2^{1+1/\beta}\cdot 3^{1/\beta}}\left[\left(12-\xi x_{+-}^{(d)}\right)\left(x_{+-}^{(d)}+2\right)^{1/\beta}\right.$$
$$\left.\left.-\left(12-\xi x_{++}^{(d)}\right)\left(x_{++}^{(d)}+2\right)^{1/\beta}\right]\right\}$$

$$F_{\text{tot}}^{(6)} = -\frac{2\pi m_0 R_s^2 \mathcal{L}_r}{\xi(2-\xi)}\left\{\frac{B_0\xi^2}{3\cdot 2^{2+\beta}}\left(\frac{B_m}{B_0}\right)^{\beta}\left[A_-\left(x_{--}^{(c)}-4\right)\left(\frac{x_{--}^{(c)}}{A_-}\right)^{\beta}\right.\right.$$
$$-A_-\left(x_{+-}^{(c)}-4\right)\left(\frac{x_{+-}^{(c)}}{A_-}\right)^{\beta} + A_+\left(x_{++}^{(c)}-4\right)\left(\frac{x_{++}^{(c)}}{A_+}\right)^{\beta}$$
$$+A_-\left(x_{+-}^{(d)}-4\right)\left(\frac{x_{+-}^{(d)}}{A_-}\right)^{\beta} - A_-\left(x_{--}^{(d)}-4\right)\left(\frac{x_{--}^{(d)}}{A_-}\right)^{\beta}$$
$$\left.\left.-A_+\left(x_{++}^{(d)}-4\right)\left(\frac{x_{++}^{(d)}}{A_+}\right)^{\beta}\right] + \frac{B_m\kappa_c^{1-1/\beta}}{2^{1+1/\beta}\cdot 3^{1/\beta}}\left[\left(12-\xi x_{--}^{(c)}\right)\right.\right.$$
$$\times\left(x_{--}^{(c)}+2\right)^{1/\beta} - \left(12-\xi x_{+-}^{(c)}\right)\left(x_{+-}^{(c)}+2\right)^{1/\beta}$$
$$+\left(12-\xi x_{++}^{(c)}\right)\left(x_{++}^{(c)}+2\right)^{1/\beta}\Big] + \frac{B_m\kappa_d^{1-1/\beta}}{2^{1+1/\beta}\cdot 3^{1/\beta}}$$
$$\times\left[\left(12-\xi x_{+-}^{(d)}\right)\left(x_{+-}^{(d)}+2\right)^{1/\beta} - \left(12-\xi x_{--}^{(d)}\right)\right.$$
$$\left.\left.\times\left(x_{--}^{(d)}+2\right)^{1/\beta} - \left(12-\xi x_{++}^{(d)}\right)\left(x_{++}^{(d)}+2\right)^{1/\beta}\right]\right\}$$

$$F_{\text{tot}}^{(7)} = -\frac{2\pi m_0 R_s^2 \mathcal{L}_r}{\xi(2-\xi)}\left\{\frac{B_0\xi^2}{3\cdot 2^{2+\beta}}\left(\frac{B_m}{B_0}\right)^{\beta}\left[A_-\left(x_{+-}^{(c)}-4\right)\right.\right.$$
$$\times\left(\frac{x_{+-}^{(c)}}{A_-}\right)^{\beta} - A_-\left(x_{--}^{(c)}-4\right)\left(\frac{x_{--}^{(c)}}{A_-}\right)^{\beta} + A_+\left(x_{++}^{(c)}-4\right)$$
$$\times\left(\frac{x_{++}^{(c)}}{A_+}\right)^{\beta} - A_+\left(x_{-+}^{(c)}-4\right)\left(\frac{x_{-+}^{(c)}}{A_+}\right)^{\beta} + A_-\left(x_{+-}^{(d)}-4\right)$$
$$\times\left(\frac{x_{+-}^{(d)}}{A_-}\right)^{\beta} - A_-\left(x_{--}^{(c)}-4\right)\left(\frac{x_{--}^{(c)}}{A_-}\right)^{\beta} - A_+\left(x_{++}^{(d)}-4\right)$$
$$\left.\left.\times\left(\frac{x_{++}^{(d)}}{A_+}\right)^{\beta} + A_+\left(x_{-+}^{(d)}-4\right)\left(\frac{x_{-+}^{(d)}}{A_+}\right)^{\beta}\right] + \frac{B_m\kappa_c^{1-1/\beta}}{2^{1+1/\beta}\cdot 3^{1/\beta}}\right.$$
$$\times\left[\left(12-\xi x_{--}^{(c)}\right)\left(x_{--}^{(c)}+2\right)^{1/\beta} - \left(12-\xi x_{+-}^{(c)}\right)\right.$$
$$\left.\times\left(x_{+-}^{(c)}+2\right)^{1/\beta} + \left(12-\xi x_{++}^{(c)}\right)\left(x_{++}^{(c)}+2\right)^{1/\beta}\right.$$

$$- \left(12 - \xi x_{--}^{(c)}\right)\left(x_{--}^{(c)} + 2\right)^{1/\beta}\Big] + \frac{B_m \kappa_d^{1-1/\beta}}{2^{1+1/\beta} \cdot 3^{1/\beta}}$$
$$\times \Big[\left(12 - \xi x_{+-}^{(d)}\right)\left(x_{+-}^{(d)} + 2\right)^{1/\beta} - \left(12 - \xi x_{--}^{(d)}\right)$$
$$\times \left(x_{--}^{(d)} + 2\right)^{1/\beta} - \left(12 - \xi x_{++}^{(d)}\right)\left(x_{++}^{(d)} + 2\right)^{1/\beta}$$
$$+ \left(12 - \xi x_{-+}^{(d)}\right)\left(x_{-+}^{(d)} + 2\right)^{1/\beta}\Big]\Bigg\} \qquad [A.6]$$

$$F_{\text{tot}}^{(8)} = -\frac{2\pi m_0 R_s^2 \mathcal{L}_r}{\xi(2-\xi)}\left\{\frac{B_0 \xi^2}{3 \cdot 2^{2+\beta}}\left(\frac{B_m}{B_0}\right)^{\beta}\Bigg[A_-\left(x_{--}^{(c)} - 4\right)\right.$$
$$\times \left(\frac{x_{--}^{(c)}}{A_-}\right)^{\beta} - A_-\left(x_{+-}^{(c)} - 4\right)\left(\frac{x_{+-}^{(c)}}{A_-}\right)^{\beta} + A_+\left(x_{++}^{(c)} - 4\right)$$
$$\times \left(\frac{x_{++}^{(c)}}{A_+}\right)^{\beta} - A_+\left(x_{-+}^{(c)} - 4\right)\left(\frac{x_{-+}^{(c)}}{A_+}\right)^{\beta} - A_+\left(x_{++}^{(d)} - 4\right)$$

**TABLE A1**
**Table of Symbols**

| Expression | Description | Note |
|---|---|---|
| $\boldsymbol{B}_0$ | External magnetic induction defining the axis of quantization and the polarization of the magnetization at a given temperature. | |
| $\boldsymbol{B}_{\text{tot}}(\boldsymbol{r})$ | Total magnetic induction at $\boldsymbol{r}$ | Section 2 |
| $\boldsymbol{F}(\boldsymbol{r}, t)$ | Local force at $\boldsymbol{r}$ | Eq. [1] |
| $\delta B$ | Intrinsic homogeneous line width | Section 2 |
| $\delta\omega$ | $\sqrt{1 + \omega_1^2 T_1 T_2}/T_2$, natural line width | |
| $\gamma$ | Gyromagnetic ratio | |
| $H_1$ | Amplitude of the rf-field | |
| $\mathcal{L}(\boldsymbol{r}, t)$ | Normalized intrinsic magnetic resonance line shape function | Eq. [8] |
| $T_1$ | Spin-lattice relaxation time | |
| $T_2$ | Spin-spin relaxation time | |
| $\omega_{\text{rf}}$ | Angular frequency of the rf-field | |
| $\omega_S(r, \theta)$ | Local angular resonance frequency of the spin system | |
| $\lvert\nabla B\rvert$ | Magnitude of the field gradient generated by the micromagnet mounted on the mechanical resonator | Eq. [2] |
| $\boldsymbol{B}(\boldsymbol{r})$ | Magnetic induction at $\boldsymbol{r}$ generated by the micromagnet | Eq. [5] |
| $B_m = 4\pi/3 \cdot M_0$ | $M_0$ is the saturation magnetization of the micromagnet | Eq. [5] |
| $R_S$ | Radius of the micromagnet in the dipolar approximation | Eq. [5] |
| $\xi$ | $B(r) = B_m(R_s/r)^{\xi}$ | Eq. [5] |
| $\beta$ | $2/\xi$ | |
| $x$ | $3\cos(2\theta) + 1$ | Eq. [12] |
| $a$ | Distance from the center of the micromagnet to the surface of the sample | Fig. 2 |
| $d$ | Thickness of a magnetic/spin layer | Fig. 5 |
| $\boldsymbol{B}_{\text{local}}(\boldsymbol{r})$ | Local magnetic induction due to internal sources such as dipolar fields | |
| $B_{c,d}(x) = B_m\left(\frac{x+2}{6\kappa_{c,d}}\right)^{\xi/2}$<br>$\kappa_c = (a/R_s)^2$<br>$\kappa_d = (a+d)^2/R_S^2$ | Sample surface in the generalized coordinate system $(B, x)$ | Eqs. [14] and [25] |
| $m_0$ | Sample magnetization density | Eq. [8] |
| $\boldsymbol{m}(\boldsymbol{r}, t)$ | Local magnetic moment at $\boldsymbol{r}$ | Eq. [1] |
| $F_{\text{tot}}$ | Total force acting on the mechanical resonator | Eq. [13] |
| $k$ | Spring constant of the mechanical resonator | |
| $Q$ | Quality factor of the magnetic resonator | |
| $z_G(t)$ | Greens function of the mechanical resonator | Eq. [15] |
| $z(t)$ | Displacement of the mechanical resonator | Eq. [15] |
| $\omega_{\text{mr}}$ | Angular frequency of the mechanical resonator | Section 2 |
| $\Gamma \simeq \omega_{\text{mr}}/(2Q)$ | Damping constant of the mechanical resonator | Eq. [15] |
| $A_{\pm} =$ | $(\omega_{\text{rf}} \pm \delta\omega/\omega_0) - 1$ | Eq. [21] |
| $B_{\pm}(x) = 2B_0 A_{\pm}/x$ | Border of the sensitive slice | Eq. [A.1] |
| $x_{\text{sl}} \approx \delta B/\lvert\nabla B\rvert$ | Spatial width of the sensitive slice | Section 5 |
| $x_{\mp\pm}^{(\alpha)} =$ | $-1 \mp \sqrt{1 + \kappa_\alpha(12B_0 A_{\pm}/B_m)}$, $\alpha = c, d$ | Eq. [23] |

*Note.* Angular frequencies and fields are related via $\omega_\alpha = \gamma B_\alpha$, where $\gamma$ is the gyromagnetic ratio and these are used interchangeably throughout the paper.

$$\times \left(\frac{x_{++}^{(d)}}{A_+}\right)^{\beta} + A_+\left(x_{-+}^{(d)} - 4\right)\left(\frac{x_{-+}^{(d)}}{A_+}\right)^{\beta}\Bigg] + \frac{B_m \kappa_c^{1-1/\beta}}{2^{1+1/\beta}\cdot 3^{1/\beta}}$$
$$\times \left[\left(12 - \xi x_{--}^{(c)}\right)\left(x_{--}^{(c)} + 2\right)^{1/\beta} - \left(12 - \xi x_{+-}^{(c)}\right)\right.$$
$$\times \left(x_{+-}^{(c)} + 2\right)^{1/\beta} + \left(12 - \xi x_{++}^{(c)}\right)\left(x_{++}^{(c)} + 2\right)^{1/\beta}$$
$$\left. - \left(12 - \xi x_{-+}^{(c)}\right)\left(x_{-+}^{(c)} + 2\right)^{1/\beta}\right] - \frac{B_m \kappa_d^{1-1/\beta}}{2^{1+1/\beta}\cdot 3^{1/\beta}}$$
$$\times \left[\left(12 - \xi x_{++}^{(d)}\right)\left(x_{++}^{(d)} + 2\right)^{1/\beta}\right.$$
$$\left. - \left(12 - \xi x_{+-}^{(d)}\right)\left(x_{+-}^{(d)} + 2\right)^{1/\beta}\right]\Bigg\}$$

$$F_{\text{tot}}^{(9)} = -\frac{2\pi m_0 R_s^2 \mathcal{L}_r}{\xi(\xi - 2)}\left\{\frac{B_0 \xi^2}{3\cdot 2^{2+\beta}}\left(\frac{B_m}{B_0}\right)^{\beta}\right.$$
$$\times \left[A_-\left(4 - x_{+-}^{(c)}\right)\left(\frac{x_{+-}^{(c)}}{A_-}\right)^{\beta} - A_-\left(4 - x_{--}^{(c)}\right)\left(\frac{x_{--}^{(c)}}{A_-}\right)^{\beta}\right.$$
$$\left. - A_+\left(4 - x_{++}^{(c)}\right)\left(\frac{x_{++}^{(c)}}{A_+}\right)^{\beta} + A_+\left(4 - x_{-+}^{(c)}\right)\left(\frac{x_{-+}^{(c)}}{A_+}\right)^{\beta}\right]$$
$$+ \frac{B_m \kappa_c^{1-1/\beta}}{2^{1+1/\beta}\cdot 3^{1/\beta}}\left[-\left(12 - \xi x_{+-}^{(c)}\right)\left(x_{+-}^{(c)} + 2\right)^{1/\beta}\right.$$
$$+ \left(12 - \xi x_{--}^{(c)}\right)\left(x_{--}^{(c)} + 2\right)^{1/\beta} + \left(12 - \xi x_{++}^{(c)}\right)$$
$$\left.\times \left(x_{++}^{(c)} + 2\right)^{1/\beta} - \left(12 - \xi x_{-+}^{(c)}\right)\left(x_{-+}^{(c)} + 2\right)^{1/\beta}\right]\Bigg\}$$

$$F_{\text{tot}}^{(10)} = -\frac{2\pi m_0 R_s^2 \mathcal{L}_r}{\xi(\xi - 2)}\left\{\frac{B_0 \xi^2}{3\cdot 2^{2+\beta}}\left(\frac{B_m}{B_0}\right)^{\beta}\left[A_+\left(x_{++}^{(c)} - 4\right)\right.\right.$$
$$\left.\times \left(\frac{x_{++}^{(c)}}{A_+}\right)^{\beta} - A_+\left(x_{-+}^{(c)} - 4\right)\left(\frac{x_{-+}^{(c)}}{A_+}\right)^{\beta}\right] + \frac{B_m \kappa_c^{1-1/\beta}}{2^{1+1/\beta}\cdot 3^{1/\beta}}$$
$$\times \left[\left(12 - \xi x_{++}^{(c)}\right)\left(x_{++}^{(c)} + 2\right)^{1/\beta} - \left(12 - \xi x_{-+}^{(c)}\right)\right.$$
$$\left.\left. \times \left(x_{-+}^{(c)} + 2\right)^{1/\beta}\right]\right\}$$

$$F_{\text{tot}}^{(11)} = 0.$$

## ACKNOWLEDGMENTS

This work was supported by the U.S. Department of Energy through the Office of Basic Energy Sciences and the Los Alamos National Laboratory Directed Research and Development. One of us (A.S.) is grateful for the partial financial support of the Swiss National Science Foundation.

## REFERENCES

1. G. Navon, Y.-Q. Song, T. Room, S. Appelt, R. E. Taylor, and A. Pines, *Science* **271,** 1848 (1996).
2. R. Tycko, S. Barrett, G. Dabbagh, L. Pfeiffer, and K. West, *Science* **268,** 1460 (1995).
3. J. M. Kikkawa and D. D. Awschalom, *Science* **287,** 473 (2000).
4. Y. S. Greenberg, *Rev. Mod. Phys.* **70,** 175 (1998).
5. J. A. Sidles, *Appl. Phys. Lett.* **58,** 2854 (1991).
6. J. A. Sidles, J. L. Garbini, K. J. Bruland, D. Rugar, O. Züger, S. Hoen, and C. S. Yannoni, *Rev. Mod. Phys.* **67,** 249 (1995).
7. D. Rugar, C. S. Yannoni, and J. A. Sidles, *Nature* **360,** 563 (1992).
8. D. Rugar, O. Züger, S. T. Hoen, C. S. Yannoni, H.-M. Vieth, and R. Kendrick, *Science* **264,** 1560 (1994).
9. Z. Zhang, P. C. Hammel, and P. E. Wigen, *Appl. Phys. Lett.* **68,** 2005 (1996).
10. O. Züger and D. Rugar, *Appl. Phys. Lett.* **63,** 2496 (1993).
11. P. C. Hammel, Z. Zhang, G. J. Moore, and M. L. Roukes, *J. Low Temp. Phys.* **101,** 59 (1995).
12. O. Züger and D. Rugar, *Appl. Phys. Lett.* **68,** 2005 (1996).
13. A Schaff and W. S. Veeman, *Appl. Phys. Lett.* **70,** 2598 (1997).
14. B. J. Suh, P. C. Hammel, Z. Zhang, M. M. Midzor, M. L. Roukes, and J. R. Childress, *J. Vac. Sci. Technol.* **16,** 2275 (1998).
15. M. Ascoli, P. Baschieri, C. Frediani, L. Lenci, M. Martinelli, G. Alzetta, R. M. Celli, and L. Pardi, *Appl. Phys. Lett.* **69,** 3920 (1996).
16. K. Wago, O. Züger, R. Kendrick, C. S. Yannoni, and D. Rugar, *J. Vac. Sci. Technol. B* **14,** 1197 (1996).
17. K. Wago, O. Züger, J. Wegener, R. Kendrick, C. S. Yannoni, and D. Rugar, *Rev. Sci. Instrum.* **68,** 1823 (1997).
18. K. Wago, D. Botkin, C. S. Yannoni, and D. Rugar, *Phys. Rev. B* **57,** 1108 (1998).
19. K. Wago, D. Botkin, C. S. Yannoni, and D. Rugar, *Appl. Phys. Lett.* **72,** 2757 (1998).
20. K. J. Bruland, W. G. Dougherty, J. L. Garbini, J. A. Sidles, and S. H. Chao, *Appl. Phys. Lett.* **73,** 3159 (1998).
21. A. Schaff and W. S. Veeman, *J. Magn. Res.* **126,** 200 (1997).
22. R. Verhagen, C. W. Hilbers, A. P. M. Kentgens, L. Lenci, R. Groeneveld, A. Wittli, and H. van Kempen, *Phys. Chem. Chem. Phys.* **1,** 4025 (1999).
23. O. Klein, V. V. Naletov, and H. Alloul, *Eur. Phys. J. B* **17,** 57 (2000).
24. O. Züger and D. Rugar, *J. Appl. Phys.* **75,** 6211 (1994).
25. A. Abragam, "The Principles of Nuclear Magnetism," Clarendon, Oxford (1961).
26. From Sigma–Aldrich, Product Number: 257621.
27. The cantilevers are commercially available from Silicon-MDT Ltd., POB 50, 103305, Moscow, Russia; http://www.siliconmdt.com/, Product Number: SC12 cont. E.
28. J. A. Sidles, J. L. Garbini, and G. P. Drobny, *Rev. Sci. Instrum.* **63,** 3881 (1992).
29. G. P. Berman, F. Borgonovi, G. Chapline, S. A. Gurvitz, P. C. Hammel, D. V. Pelekhov, A. Suter, and V. I. Tsifrinovich, http: //xxx.lanl.gov/abs/quant-ph/0101035 (2001).